

# Light-Induced Degradation of Thin-film Silicon Solar Cell Absorbers

WANG PO KANG

Delft University of Technology

# Light-Induced Degradation of Thin-film Silicon Solar Cell Absorbers

by

WANG PO KANG

to obtain the degree of Master of Science  
at the Delft University of Technology,  
to be defended publicly on Wednesday 16 July, 2024 at 15:00 pm

Thesis committee:

Prof. dr. ir. Arno Smets

Prof. Hesam Ziar

Prof. Simon Tindemans

Ir. Govind Padmakumar,

Faculty:

Faculty of Sustainable Electrical Engineering, Delft

# Abstract

Multi-junction solar cells, particularly those that combine amorphous silicon (a-Si) and nanocrystalline silicon (nc-Si) materials, represent a promising strategy to boost the efficiency of solar energy conversion. By integrating a-Si and nc-Si layers within a tandem configuration, these cells optimize the utilization of the solar spectrum, effectively overcoming the limitations associated with traditional single-junction solar cells. Positioned as the top cell, the a-Si layer absorbs shorter-wavelength light, complemented by the nc-Si layer beneath it, which captures longer-wavelength photons. This synergistic absorption capability results in broader spectral coverage and significantly enhanced overall efficiency.

Although thin film silicon solar cells present numerous advantages, they are not without drawbacks and challenges. A significant issue is stability and degradation, particularly concerning the sensitivity of amorphous silicon (a-Si) to light-induced degradation.

Silicon carbide (SiC) and silicon oxide (SiO<sub>x</sub>) have garnered increased attention to reduce the parasitic absorption at the p layer when compared to p-aSi. An outstanding question is how the integration of p-SiC and p-SiO<sub>x</sub> impacts the metastability of the solar cells. Previous work in the PVMD group at TU Delft has studied the stability of the p-nc-SiO<sub>x</sub> in detail revealing from experimental results that stable efficiency remains elusive.

This thesis investigates the impact of p-a-SiC on the light-induced degradation (LID) of p-i-n solar cells, aiming to compare its degradation performance with that of p-nc-SiO<sub>x</sub>. Prior to comparison, p-a-SiC fabrication via plasma-enhanced chemical vapor deposition (PECVD) is extensively explored, as it serves as a widely used light absorber in thin-film silicon solar cells. Various parameters such as power pressure and gas flow rate of the source gas for silicon carbide formation are meticulously studied to achieve optimal p-a-SiC performance. Once the optimal fabrication conditions are identified, light absorption experiments are conducted and characterized using JV and EQE measurements to assess LID performance.

# Contents

<b>Abstract</b>	<b>i</b>
<b>1 Introduction</b>	<b>1</b>
1.1 Thin-film technology	1
1.2 Silicon Carbide and Silicon Oxide layers	2
1.3 Research questions	2
1.4 Thesis outline	3
<b>2 Fundamentals</b>	<b>4</b>
2.1 Fundamentals of solar cell	4
2.1.1 Loss mechanisms	5
2.2 Fundamentals of amorphous silicon	6
2.2.1 Configuration of amorphous silicon	6
2.2.2 Crystallinity of a-Si and nc-Si	7
2.2.3 Energy Level Distribution	8
2.2.4 Structural imperfections in hydrogenated amorphous silicon	9
2.2.5 The Staebler-Wronski effect	10
2.3 Single junction solar cell	10
2.4 Multi-junction a-Si:H solar cells	11
2.5 Fabrication techniques	13
2.5.1 Plasma Enhanced Chemical Vapour Deposition (PECVD)	13
2.6 Characterization processes	14
2.6.1 Current-voltage measurement	14
2.6.2 External quantum efficiency measurement	14
2.6.3 Spectroscopic Ellipsometry	15
2.6.4 Dark conductivity	16
2.6.5 Reflectance measurement	17
<b>3 The fabrication of Boron doped Silicon Carbide with PECVD</b>	<b>18</b>
3.1 Introduction	18
3.2 Background study	19
3.2.1 SiC and SiO <sub>x</sub>	19
3.2.2 PECVD	20
3.3 Methodology	20
3.3.1 Film deposition	20
3.3.2 Design of experiments	20
3.4 Results and Discussion	21
3.4.1 Optical and electrical performance	21
3.5 Results of optimization of p-SiC	25
3.6 Discussion	26
<b>4 LID study of Different Solar cell Architectures</b>	<b>27</b>
4.1 Introduction	27
4.2 Background study	27
4.2.1 Proposed theories on SWE	28
4.2.2 Deposition Conditions and Their Impact on LID	30
4.2.3 Effects of Thermal Annealing	30
4.3 Methodology	31
4.3.1 Configurations of cells	31
4.3.2 Initial performance	33
4.3.3 Light soaking experiment	33

---

4.4	Design of experiments . . . . .	34
4.5	Results and Discussion . . . . .	35
4.5.1	LID on Solar cells with p doped Silicon Carbide as Window layer . . . . .	35
4.5.2	Effects of Light Exposure on Nanocrystalline Single Junction Solar cells . . . . .	39
4.5.3	LID on Solar cells with p-nc-SiO <sub>x</sub> as window layer on micromorph thin film . . . . .	43
4.6	Summary . . . . .	46
<b>5</b>	<b>Conclusions and Recommendations</b>	<b>48</b>
5.1	Conclusions . . . . .	48
5.2	Recommendations . . . . .	48
	<b>References</b>	<b>50</b>

# List of Figures

2.1	The absorption of a photon in a semiconductor [15]. . . . .	4
2.2	The model illustrates generation, recombination, and absorption of solar cells [15]. . . . .	5
2.3	The absorber efficiency A, the thermodynamic efficiency TD, and the combined solar cell efficiency SC under full concentration are illustrated for a solar temperature of 5,800 K and an ambient temperature of 300 K [18]. . . . .	6
2.4	Atomic structure of (a) crystalline silicon and (b) hydrogenated amorphous silicon [19]. . . . .	7
2.5	The silicon phases between nanocrystalline and amorphous solar cells [15]. . . . .	8
2.6	distribution of density of allowed energy states for electrons for (a) single crystal silicon (b) a-Si:H [15]. . . . .	8
2.7	nanostructures in a-Si:H bulk [25]. . . . .	9
2.8	Fill factor degradation after light induce degradation [15]. . . . .	10
2.9	Architecture of single junction solar cell with superstrate p-i-n configuration [29]. . . . .	11
2.10	Spectral utilization of Multi-junction solar cell [15]. . . . .	12
2.11	Device architecture of a-Si:H based multi-junction solar cell with superstrate p-i-n configuration [15]. . . . .	12
2.12	schematic representation of the PECVD [35]. . . . .	13
2.13	Control page of PECVD . . . . .	13
2.14	Tuning of reflected power. . . . .	14
2.15	schematic representation of EQE measurement [37]. . . . .	15
2.16	schematic representation of Spectroscopic Ellipsometry [38]. . . . .	15
2.17	The model of Spectroscopic Ellipsometry . . . . .	16
2.18	Schematic representation of dark conductivity [40]. . . . .	16
3.1	Optimisation of P doped silicon carbide layer for superstrate configuration . . . . .	18
3.2	EQE comparison between p-a-SiC and p-nc-SiOx . . . . .	19
3.3	JV curve between SiC and SiOx before optimization . . . . .	19
3.4	The process of fabrication and characterization for P layer . . . . .	20
3.5	Design of experiment . . . . .	21
3.6	Activation energy in different power and pressure . . . . .	22
3.7	Activation energy in different gas flow rate of diborane(B <sub>2</sub> H <sub>6</sub> ) and methane(CH <sub>4</sub> ) . . . . .	22
3.8	Dark conductivity in different power and pressure . . . . .	23
3.9	Dark conductivity in different gas flow rate of diborane(B <sub>2</sub> H <sub>6</sub> ) and methan(CH <sub>4</sub> ) . . . . .	23
3.10	Energyband gap in power and pressure . . . . .	24
3.11	Energy bandgap in different gas flow rate of diborane(B <sub>2</sub> H <sub>6</sub> ) and methan(CH <sub>4</sub> ) . . . . .	24
3.12	Refractive index in different power and pressure combinations at wavelength 900nm . . . . .	25
3.13	EQE of p-i-n solar cell including the p-a-SiC layer before and after optimization of fabrication . . . . .	25
3.14	JV curve before and after optimization . . . . .	26
4.1	he density of dangling bounds with the function of light absorption time [59]. . . . .	28
4.2	Schematic representation of a new nanoscopic model of the LID in a-si:H[60]. . . . .	29
4.3	Thickness-dependent dangling bond concentration after light exposure and thermal treatment[60]. . . . .	30
4.4	Device configuration of a-Si:H single junction solar cell with P-SiC window layer . . . . .	31
4.5	Sample with 30 cells. . . . .	31
4.6	Device configuration of a-Si:H single junction solar cell with p-nc-SiOx window layer . . . . .	32
4.7	Device configuration of nc-Si:H single junction solar cell with P-nc-SiOx window layer . . . . .	32
4.8	Device configuration of c-SiOx:H multi-junction solar cell with p-nc-SiOx window layer . . . . .	33
4.9	The set up of Light absorption experiment . . . . .	34
4.10	The flow chart of Light soaking experiment . . . . .	35

4.11	Initial performance of EQE and absorptance of SiC and SiOx . . . . .	35
4.12	EQE of LID of p-a-SiC and p-a-SiOx window layer in amorphous silicon . . . . .	36
4.13	JV curve of p-a-SiC and p-nc-SiOx window layer in amorphous silicon . . . . .	36
4.14	Fill factor for p-a-SiC and p-nc-SiOx window layer in amorphous silicon . . . . .	37
4.15	Fill factor for p-nc-SiOx window layer in amorphous silicon . . . . .	37
4.16	Voc for p-a-SiC and p-nc-SiOx window layer in amorphous silicon . . . . .	38
4.17	Series resistance of p-a-SiC and p-a-SiOx window layer in amorphous silicon . . . . .	38
4.18	Shunt resistance of p-a-SiC and p-a-SiOx window layer in amorphous silicon . . . . .	39
4.19	Efficiency of p-a-SiC and p-a-SiOx window layer in amorphous silicon . . . . .	39
4.20	Initial performance of EQE and absorptance of TCO(IOH) and bilayer TCO(IOH+iZnO) layers . . . . .	40
4.21	EQE of TCO(IOH) and bilayer TCO(IOH+iZnO) after degradation. . . . .	40
4.22	JV of TCO(IOH) and TCO (IOH+iZnO) layers . . . . .	41
4.23	FF of TCO(IOH) and (IOH+iZnO) layers . . . . .	41
4.24	Voc of TCO(IOH) and (IOH+iZnO) layers . . . . .	42
4.25	Series resistance of TCO(IOH) and (IOH+iZnO) layers . . . . .	42
4.26	Shunt resistance of TCO(IOH) and (IOH+iZnO) layers . . . . .	43
4.27	Efficiency of TCO(IOH) and (IOH+iZnO) layers . . . . .	43
4.28	EQE for micromorph thin-film . . . . .	44
4.29	Fill factor for micromorph thin-film . . . . .	45
4.30	Open voltage for micromorph thin-film . . . . .	45
4.31	Series resistance for micromorph thin film . . . . .	46
4.32	Shunt resistance for micromorph thin film . . . . .	46

# Introduction

## 1.1. Thin-film technology

The development of crystalline silicon (c-Si) solar cells began in 1954 when Bell Labs produced the first functional photovoltaic (PV) cell. This pioneering cell, made from crystalline silicon, achieved an efficiency of approximately 6%, marking a crucial breakthrough in harnessing sunlight for electricity. This innovation laid the foundation for future solar technology advancements. [1]. For more than three decades, crystalline silicon (c-Si) has maintained its leading position in the solar market due to several key factors. First, efficiency: monocrystalline silicon cells, in particular, deliver high-efficiency levels, often surpassing 20%, making them a dependable option for a wide range of applications. Secondly, durability: crystalline silicon panels are known for their long-term stability and robustness, consistently delivering reliable performance for over 25 years. Lastly, cost reduction: improvements in manufacturing techniques and economies of scale have substantially decreased production costs, making c-Si cells more affordable and widely available. Thanks to these advantages, crystalline silicon has remained dominant in the market for more than 30 years[2].

On the other hand, thin-film solar cells are a kind of photovoltaic cell created by layering one or more thin films of photovoltaic material onto a base. These cells are recognized for their lightweight nature, flexibility, and lower production costs compared to traditional silicon-based cells. The main materials used in thin-film cells are amorphous silicon (a-Si), Cadmium Telluride (CdTe), and Copper Indium Gallium Selenide (CIGS). Due to their flexible and lightweight properties, thin-film cells are often utilized in scenarios where these characteristics are crucial, such as in building-integrated photovoltaics and portable solar devices.[3].

Thin-film solar cells come in various types, with CdTe being a prominent material in this category. CdTe has long dominated the thin-film solar panel market due to its effectiveness in converting sunlight into electricity and its comparatively low manufacturing costs. Recent data indicates that CdTe accounts for roughly 50% of the global market share in thin-film photovoltaic technologies [4]. Nonetheless, cadmium is a highly toxic heavy metal, and its use in CdTe solar panels poses significant environmental and health concerns [5]. Secondly, CIGS is a significant player in the thin-film solar cell market, though it holds a smaller share compared to CdTe. As of recent estimates, CIGS accounts for about 10-15% of the global thin-film solar market [4]. The drawback of CIGS solar cells is that they use rare and expensive materials like indium and gallium. These materials contribute to the high production costs of CIGS panels.

Finally, amorphous silicon (a-Si) solar cells, while still holding a notable portion of the market, have been experiencing a decline in comparison to other technologies. Recent estimates suggest that a-Si solar cells currently represent about 5-10% of the global thin-film solar market.[4]. The market share of a-Si cells has gradually declined as they face increasing competition from other thin-film technologies such as CdTe and CIGS. One key benefit of a-Si cells is their minimal silicon usage compared to crystalline silicon cells, which helps reduce production costs. Additionally, the manufacturing process for a-Si is simpler and requires less energy than that of crystalline silicon cells [6].

Another major benefit of amorphous silicon (a-Si) solar cells is their flexibility and lightweight design. These cells can be applied to flexible substrates, making them ideal for uses such as solar fabrics and building-integrated materials. Additionally, their lighter weight compared to traditional silicon panels simplifies handling and installation.[7]. Despite their advantages, a-Si cells typically have lower energy conversion efficiencies than crystalline silicon cells. Their efficiency usually falls between 6-10%, which is considerably less than that of crystalline silicon cells [4].

Additionally, a-Si cells are affected by the Staebler-Wronski effect, a phenomenon where their efficiency declines after extended exposure to light[8]. These drawbacks have hindered the further development of a-Si cells.

## 1.2. Silicon Carbide and Silicon Oxide layers

Edward G. Acheson discovered silicon carbide while attempting to create synthetic diamonds. He named the material "Carborundum" and patented the process for its production. The Acheson process involved heating a mixture of clay (silica) and carbon (coke) in an electric furnace.[9]

First, silicon carbide was valued in industrial settings for its remarkable hardness and abrasive qualities. It was extensively used in grinding wheels, cutting tools, and sandpaper abrasives. Nevertheless, it wasn't until the mid-20th century that its full potential as a semiconductor material began to be recognized.

In the 1950s and 1960s, researchers began exploring the semiconductor properties of silicon carbide (SiC). They discovered that SiC has a broad bandgap, ranging from about 2.2 eV to 3.3 eV depending on its crystal structure or polytype. This wide bandgap enables SiC to operate efficiently at higher temperatures and handle greater voltages than traditional silicon (Si) semiconductor materials.[10]

With the advancement of the semiconductor industry, silicon carbide (SiC) began to be acknowledged for its advantages in high-power and high-temperature applications. During the 1980s and 1990s, significant progress was made in SiC crystal growth and device manufacturing techniques. These developments allow the creation of high-quality SiC crystals with few defects, paving the way for their application in power electronics, LEDs, and, more recently, solar cells and optoelectronics. [11]

The use of silicon dioxide (SiO<sub>2</sub>) as a gate dielectric in Metal-Oxide-Semiconductor (MOS) transistors marked a pivotal change in the semiconductor field. This breakthrough enabled the miniaturization of transistors and sped up the advancement of integrated circuit (IC) technology. As a result, it greatly enhanced computing power and contributed to the extensive spread of electronic devices toward the end of the 20th century.[12]

Throughout the years, scientists have progressively improved the methods for depositing SiO<sub>x</sub> layers, such as thermal oxidation, chemical vapor deposition (CVD), and plasma-enhanced CVD (PECVD). These advanced techniques provide accurate control over the thickness and characteristics of SiO<sub>x</sub> films, which is crucial for producing sophisticated semiconductor devices with nanoscale dimensions.

## 1.3. Research questions

Significant advancements and research efforts have been made in amorphous silicon-based thin-film solar cell technology, focusing on deposition conditions, techniques, material utilization, and device configuration. Despite these strides, a notable challenge known as the Staebler-Wronski Effect (SWE) persists.

The PVMD group at TU Delft has conducted extensive research into optimizing the Staebler-Wronski Effect over many years. One previous research focus was on studying how the p-nc-SiO<sub>x</sub> layer influences the Light Induced Degradation (LID) of p-i-n solar cells. According to experimental findings, the p-nc-SiO<sub>x</sub> layer continues to experience LID and did not achieve stable efficiency even after 1000 hours of light exposure.

As mentioned before, the main reason for using these SiO<sub>x</sub> and SiC is to reduce the parasitic absorption at the p-layer when compared to p-aSi. This thesis explores the impact of a P-SiC layer on the Light Induced Degradation (LID) of p-type amorphous silicon solar cells. Our group is particularly interested in comparing LID performance between p-nc-SiO<sub>x</sub> and p-a-SiC to determine if stable efficiency can be achieved by applying a p-SiC layer. Before conducting comparisons, it is essential to optimize the fabrication process of p-SiC to ensure optimal layer performance.

Furthermore, we are applying a p-nc-SiO<sub>x</sub> window layer in a-Si, nc-Si, and micromorph cell to assess their performance in light-induced degradation. Given the occurrence of the Staebler–Wronski Effect (SWE) in amorphous silicon, we aim to investigate if two nc-Si samples using different types of transparent conducting oxide (iOH and bi TCO) still exhibit light-induced degradation. Additionally, three samples of micromorph cell with varying combinations of current density for the top and bottom cells are being studied in light absorption experiments to determine which current density combination yields the best performance. The micromorph thin film use a-Si as the intrinsic layer of top cell and nc-Si as the intrinsic layer of bottom cell.

**This thesis will answer the following research questions:**

1. How do the material properties of boron-doped amorphous silicon carbide depend on the PECVD deposition conditions? which P-SiC layers, when integrated into as p-layer into an amorphous silicon solar cell result in the best device performance?
2. How does the boron-doped silicon carbide when used in a front p-doped layer affect the LID of amorphous silicon single junction solar cells?
3. How do nanocrystalline single junction solar cells degrade under light exposure ?
4. How to implement fill factor compensation techniques in multijunction solar cells?

## **1.4. Thesis outline**

This thesis comprises 5 chapters. Apart from the Introduction discussed in this section, Chapter 2 delves into fundamental knowledge about amorphous silicon and its applications. It also covers the fabrication via PECVD and characterization via SE and conductivity measurement relevant to this thesis. Chapter 3 explores the fundamentals of light-induced degradation, along with background studies on silicon carbide and silicon oxide. Furthermore, the fabrication process of P-doped silicon carbide using PECVD. Chapter 4 explores the light-induced degradation performance of p-nc-SiO<sub>x</sub> and p-a-SiC via light absorption experiments. Moreover, the light-induced degradation performance of multiple junction solar cells is studied, and the experimental results will be presented towards the end of this chapter. Chapter 5 concludes the thesis by addressing key findings to answer the main questions posed. Additionally, recommendations for future studies are provided.

# 2

## Fundamentals

In this chapter, the theoretical framework for the thesis is established. It starts by outlining the essential principles behind solar cell technology. The chapter then focuses on the properties of amorphous silicon (a-Si). A thorough analysis of a-Si multi-junction devices is then presented, as these devices are crucial to the research objectives. Subsequent sections review the various deposition techniques employed in solar cell production. The chapter concludes by detailing the characterization techniques used throughout the study.

### 2.1. Fundamentals of solar cell

The photovoltaic effect describes how a photovoltaic cell produces a voltage or electric current upon being illuminated by sunlight[13]. This occurs when light or another type of radiant energy interacts with two distinct materials that are in close proximity, resulting in the generation of electrical voltage. In 1905, Albert Einstein clarified the photoelectric effect by proposing that light is made up of individual energy units known as photons[14]. The photovoltaic effect, based on photons as well, can be broken down into three primary stages:

1. The generation of charge carriers occurs when photons are absorbed by the materials forming the junction.
2. Separating the charge carriers created by the absorbed photons within the junction.
3. Collecting the charge carriers generated by the photons at the junction's terminals.

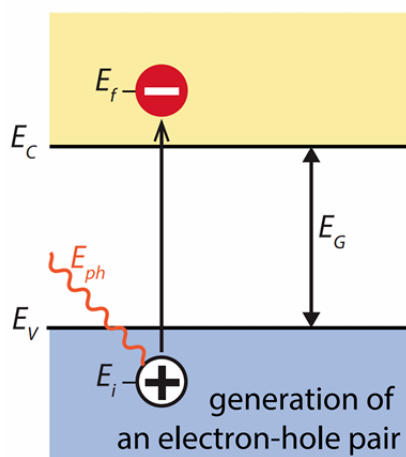


Figure 2.1: The absorption of a photon in a semiconductor [15].

Figure 2.1 illustrates When a material absorbs a photon, the energy of the photon elevates an electron from a lower energy band to a higher one. This transition happens only if the energy of the photon is greater than the material's band gap energy,  $E_G$ . The electron energy levels,  $E_c$  and  $E_v$ , are arranged so that the difference between them,  $E_G = E_c - E_v$ , corresponds to the energy of the photon ( $h\nu$ )[15].

In semiconductors, the energy levels of the valence and conduction bands are not uniform but instead vary with the  $k$ -vector, which represents the momentum of an electron (or hole) within a crystal lattice and relates to the wavelength of the electron's wave-like behavior. This variation implies that an electron's energy depends on its momentum due to the periodic nature of the semiconductor crystal. If the highest energy point in the valence band and the lowest energy point in the conduction band align at the same  $k$ -vector, electrons can transition between these bands without altering their momentum, classifying the semiconductor as a direct band gap material. Conversely, if such a transition requires a change in momentum, the semiconductor is referred to as an indirect band gap material. [16]

### Separating the charge carriers created by the absorbed photons within the junction.

As depicted in Figure 2.2, usually, the electron-hole pair will recombine, with the electron falling back to its previous energy state. This recombination can either release energy as a photon (radiative recombination) or transfer energy to other electrons, holes, or lattice vibrations (non-radiative recombination)[15].

For a solar cell to effectively convert the energy from electron-hole pairs into work in an external circuit, it must be engineered so that electrons and holes reach the electrodes before they have a chance to recombine. This requires that the time it takes for charge carriers to travel to the electrodes be less than their recombination lifetime, which limits the thickness of the absorber layer.

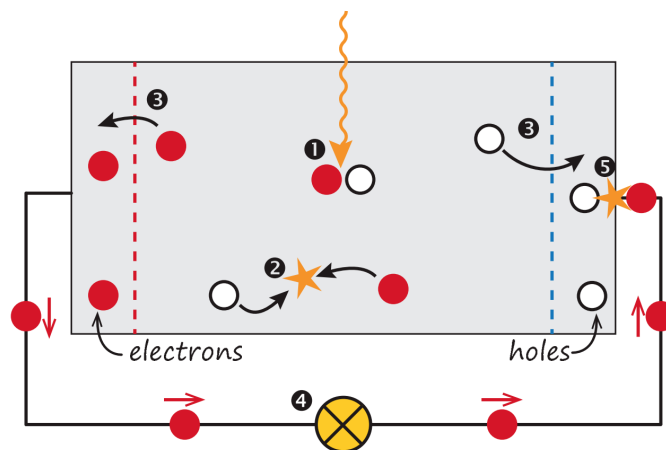


Figure 2.2: The model illustrates generation, recombination, and absorption of solar cells [15].

### Collecting the charge carriers generated by the photons at the junction's terminals

In the last phase, electrical contacts draw out the charge carriers from the solar cells, allowing them to do work within an external circuit. This process converts the chemical energy of the electron-hole pairs into electrical energy. As the electrons move through the circuit, they eventually recombine with holes at the interfaces between the metal and the absorber. This process is depicted in Figure 2.2.

#### 2.1.1. Loss mechanisms

In single-junction solar cells, there are two primary sources of energy loss: first, photons with energies below the bandgap cannot be converted into electricity; second, photons with energies higher than the bandgap result in thermalization losses. This usually leads to more than 50% loss depending on the bandgap of the semiconductor. [17]

The fundamental limitation arises from the thermodynamic boundary. Solar cells function as devices that convert energy quantum-mechanically and are therefore bound by the limits of thermodynamic efficiency. Energy exceeding the bandgap gets converted into kinetic energy during carrier recombination.

This additional kinetic energy is eventually released as heat through interactions with phonons, as the carriers settle back to their equilibrium speeds. As a result, there is a natural limit beyond which solar energy cannot be effectively converted into electrical power[18].

Figure Figure 2.3 depicts the efficiency of the absorber. When comparing the thermodynamic efficiency to that of solar cells, it becomes evident that a solar cell can achieve a maximum efficiency of approximately 85% at an absorber temperature of 2,480 K. Despite this, this efficiency is still significantly below the thermodynamic limit. For a thorough exploration of this thermodynamic limit, readers are encouraged to refer to the research conducted by Würfel et al. [18]

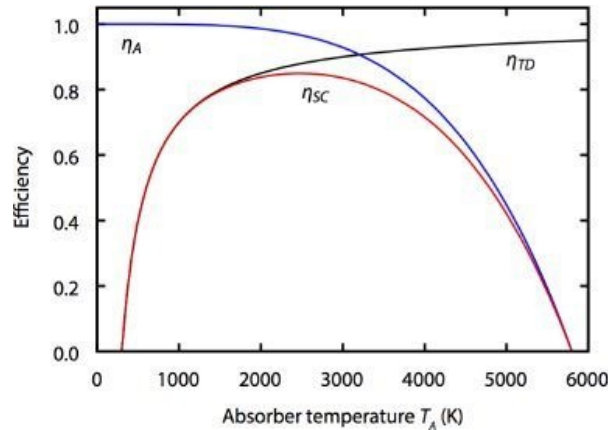


**Figure 2.3:** The absorber efficiency A, the thermodynamic efficiency TD, and the combined solar cell efficiency SC under full concentration are illustrated for a solar temperature of 5,800 K and an ambient temperature of 300 K [18].

## 2.2. Fundamentals of amorphous silicon

Hydrogenated amorphous silicon (a-Si:H) has garnered significant interest due to its potential for producing cost-effective solar cells. Additionally, a-Si has been crucial for many years as the intrinsic absorber layer in combination with doped layers, to create PIN junctions. To fully grasp its role in solar cells and how it differs from traditional crystalline silicon (c-Si) cells, it is important to understand the material properties of a-Si.

### 2.2.1. Configuration of amorphous silicon

The Figure 2.4 illustrates the structural differences between c-Si and a-Si. Unlike crystalline silicon (c-Si), which has a well-ordered atomic arrangement, amorphous silicon (a-Si) lacks long-range order. In a-Si, silicon atoms are arranged in a random, disordered manner rather than forming a consistent, repeating pattern as in crystals. This randomness causes variations in bond lengths and angles between adjacent atoms, resulting in localized structural inconsistencies within the material[19].

Amorphous silicon stands apart from crystalline silicon due to its distinctly disordered atomic structure, which lacks the long-range periodicity found in crystalline forms. While crystalline silicon features a regular, repeating lattice arrangement, amorphous silicon displays a more random and irregular atomic distribution. Additionally, the inclusion of hydrogen is vital for improving the electronic characteristics of amorphous silicon[19].

In the amorphous silicon lattice, silicon atoms bond together, but due to the lack of a structured arrangement, there are more defects and dangling bonds than in crystalline silicon. These imperfections create additional electronic states within the band gap, which notably affect the material's electrical properties.[20].

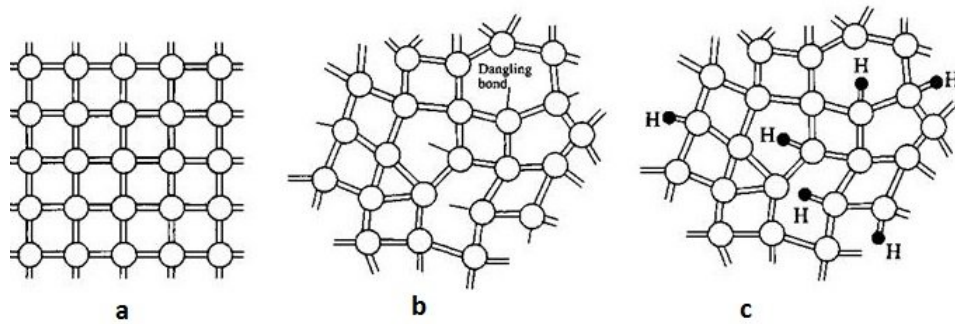


Figure 2.4: Atomic structure of (a) crystalline silicon and (b) hydrogenated amorphous silicon [19]

To address this issue, amorphous silicon undergoes a process called hydrogenation, where hydrogen atoms attach to dangling bonds, thereby neutralizing defects. A passivated dangling bond, where hydrogen has bonded, is represented by a small black circle at the end. Hydrogenation is often abbreviated with an 'H' following a colon, though for simplicity, the term 'hydrogenated' is frequently left out. This hydrogen treatment drastically lowers the defect density in amorphous silicon films by about three orders of magnitude.

In amorphous silicon, dangling bonds are usually not evenly spread but tend to aggregate into small clusters. These clusters can lead to the formation of common defects such as monovacancies, divacancies, and nanoscale voids with diameters in the range of several nanometers. The surfaces of these nanoscale voids are mostly covered with monohydride. Occasionally, within these voids, a silicon atom might bond with only two neighboring silicon atoms. These two dangling bonds are then passivated by two hydrogen atoms, resulting in what is known as dihydride silicon atoms.[21].

### 2.2.2. Crystallinity of a-Si and nc-Si

To comprehend the distinction between a-Si and nc-Si, it is essential to delve into the silicon phases. nc-Si, also referred to as microcrystalline silicon, constitutes a hydrogenated silicon alloy with a highly intricate structure. This phase comprises small grains, typically a few tens of nanometers in size, each possessing a crystalline lattice[15]. The diagram in Figure 2.5 visually represents this silicon phase: yellow regions denote crystalline grains, while brown regions indicate the amorphous matrix.

The crystalline volume fraction of the deposited film varies depending on the specific conditions employed during chemical vapor deposition. On one end of the spectrum, a fully crystalline phase can be observed, resembling Polycrystalline silicon but with additional cracks and pores in the material[15]. The proportion of crystalline volume decreases progressively from left to right in the illustration, with the material becoming fully amorphous on the right-hand side. The degree of crystallinity quantifies the volume fraction occupied by the crystalline phase relative to the total silicon volume. Depending on the deposition conditions, nanocrystalline material can exhibit a range of crystallinity levels: from entirely amorphous, through a mixed phase containing small crystalline grains, to a phase predominantly composed of large crystalline grains with minimal amorphous content.

Research indicates that the most effective nanocrystalline materials used in solar cells typically exhibit a structure close to the boundary between nanocrystalline and amorphous silicon, with a crystallinity around 60%[22].

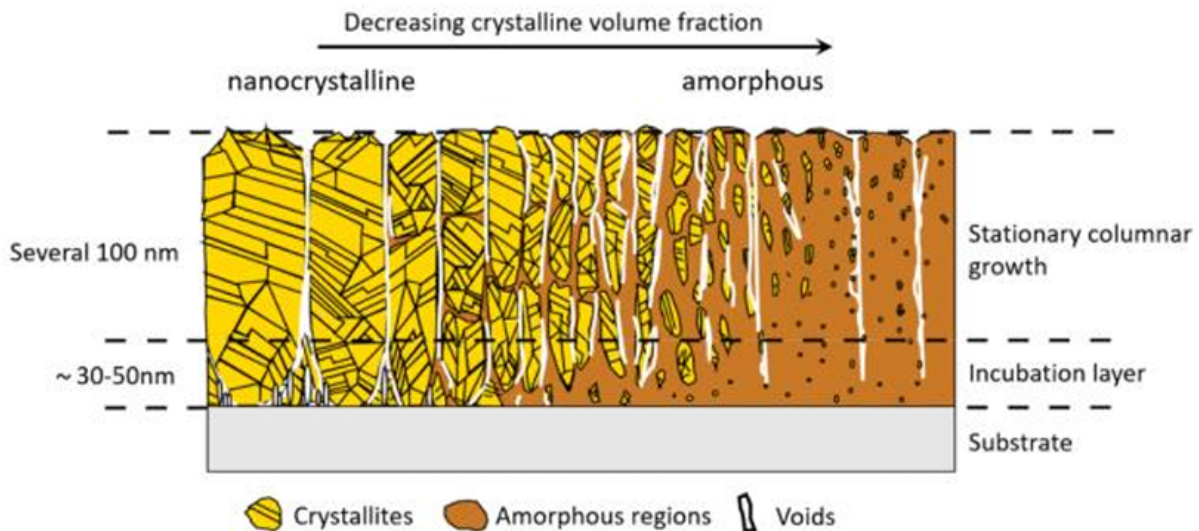


Figure 2.5: The silicon phases between nanocrystalline and amorphous solar cells [15].

### 2.2.3. Energy Level Distribution

The contrast in energy states between single-crystal silicon and hydrogenated amorphous silicon is demonstrated in Figure 2.6, emphasizing their unique atomic configurations. The figure shows that single-crystal silicon has a distinct band gap separating the valence and conduction bands, indicative of its regular atomic structure. At room temperature, this band gap ( $E_g$ ) is 1.12 eV, distinctly defining the energy levels where electron transitions can occur.

in single-crystal silicon, the density of states in hydrogenated amorphous silicon (a-Si) is continuous, with no clear band gap between the valence and conduction bands, as shown in Figure 2.3(b). The atomic disorder characteristic of a-Si leads to the formation of band tail states within the band gap. The extent of this disorder is evaluated by the width of these band tails, which expand as the disorder in the a-Si material increases.

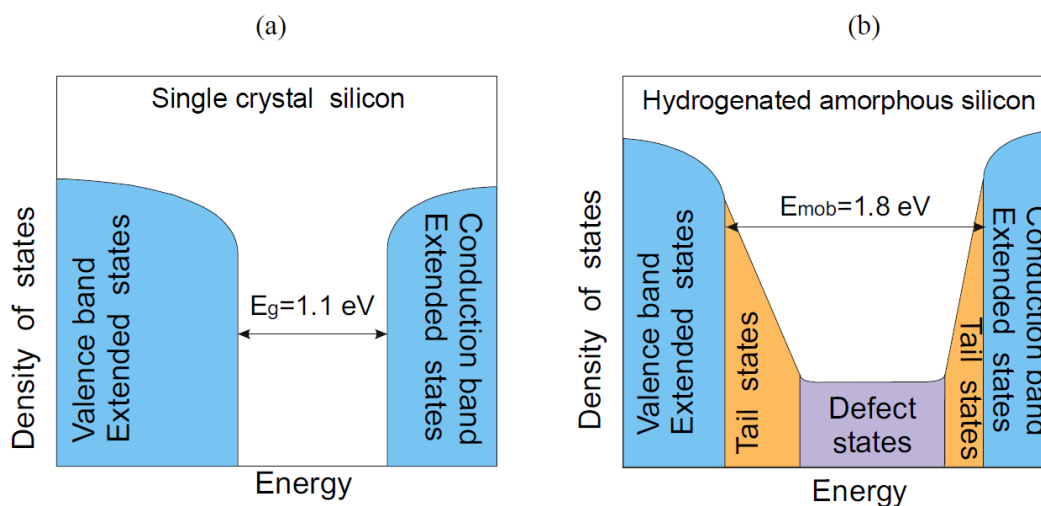


Figure 2.6: distribution of density of allowed energy states for electrons for (a) single crystal silicon (b) a-Si:H [15].

The amorphous silicon lattice is characterized by its disordered nature, where numerous defects and vacancies contribute to a wider spectrum of allowable energy states, unlike the structured crystalline lattice. These defect states introduce energy levels within the center of the forbidden gap. Due to

the absence of sharp band edges, accurately determining the band gap energy for amorphous silicon becomes challenging[15].

Overall, amorphous silicon is classified as a direct band gap material due to its abundance of permissible energy states.

#### 2.2.4. Structural imperfections in hydrogenated amorphous silicon

Structural flaws in hydrogenated amorphous silicon arise from deviations from the idealized amorphous structure, envisioned as a continuous random network (CRN) where every bond is complete: each silicon atom forms four tetrahedral bonds, and each hydrogen atom forms a single bond [23]. Based on this concept, defects in a-Si generally involve atoms being either under-coordinated or over-coordinated, a condition referred to as a coordination defect.

Several models have been employed to analyze the defects in a-Si, one of which is the disordered network with hydrogenated vacancies (DNHV)..

##### The model of Disordered network with hydrogenated vacancies (DNHV):

The disordered network with hydrogenated vacancies (DNHV) model is used to describe the structural flaws in hydrogenated amorphous silicon (a-Si). Unlike the traditional continuous random network (CRN) model, which assumes a uniform spread of defects such as dangling bonds throughout the silicon, the DNHV model suggests a different distribution pattern of these imperfections[24].

The DNHV model emphasizes the role of hydrogenated vacancies within the amorphous silicon network. These vacancies are essentially sites where a silicon atom is absent, which can either remain vacant or be occupied by hydrogen. According to this model, these vacancies, along with the hydrogen atoms that might fill them, are crucial in determining the electronic properties and stability of a-Si[24].

The DNHV model suggests that the electronic states linked to these vacancies and hydrogenated sites contribute to the density of states within the band gap of a-Si. These states influence the material's optical and electrical characteristics, such as its capacity to absorb and emit light and its charge carrier mobility.[24].

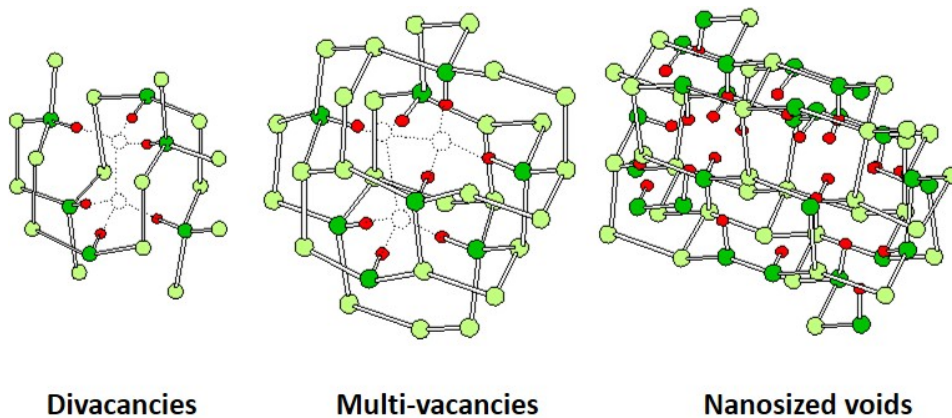


Figure 2.7: nanostructures in a-Si:H bulk [25]

These larger structural voids or defects within the silicon network are critical features of the material's architecture. Smets and Van De Sanden (2007) explore how these open volume deficiencies, coupled with the movement of hydrogen throughout the a-Si structure, shape the overall defect landscape of the material. They highlight that these deficiencies can have a profound impact on the electronic properties of a-Si by introducing extra defect states within the band gap. Their work underscores the intricate nature of a-Si's nanostructure and the essential role of hydrogen in reducing the negative effects of these defects.[23].

### 2.2.5. The Staebler-Wronski effect

The Staebler-Wronski effect (SWE) describes a phenomenon in hydrogenated amorphous silicon (a-Si) where prolonged light exposure leads to temporary changes in the material's electronic properties. Discovered by David Staebler and Christopher Wronski in 1977 [26], this effect manifests as a reversible decline in the performance of a-Si-based devices, such as solar cells and thin-film transistors, after extended light exposure. The mechanism behind the Staebler-Wronski Effect can be divided into three main components:

#### Light-Induced Defects:

When exposed to light, photons in the a-Si material generate electron-hole pairs. These carriers may get trapped at defect sites, which can either create new dangling bonds or modify existing ones. As a result, the density of defects within the material increases [27].

#### Metastable Changes:

The newly created defects are metastable, so they remain even after the light source is turned off. These defects lead to a higher rate of charge carrier recombination, which in turn diminishes the material's electrical conductivity and its effectiveness in converting light into electrical energy.

#### Reversibility:

The effects of the SWE can be partially reversed. By annealing the material to higher temperatures, usually around 150°C, it is possible to lower the defect density and partially regain the material's initial properties. This suggests that the defects caused by the SWE do not permanently damage the a-Si structure [28].

Figure 2.8 shows how the fill factor of an a-Si film decreases with prolonged light exposure. Initially, there is a sharp drop in the fill factor during the first few hours, followed by a more gradual decline as documented in the literature. This reduction can be partly reversed with thermal annealing, which improves the fill factor, indicating that annealing at temperatures above 150°C can alleviate the Staebler-Wronski Effect. Generally, the degradation process stabilizes after about 1000 hours of light exposure under standard test conditions (STC), after which the performance of the solar cell levels off for the rest of its operational life. Ensuring this performance stability is crucial for practical application of the material.

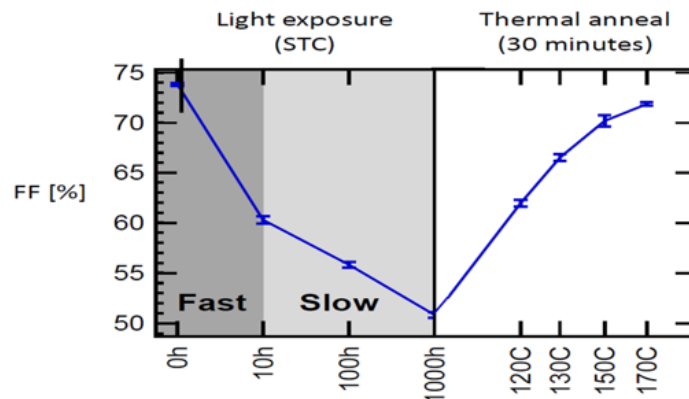


Figure 2.8: Fill factor degradation after light induce degradation [15]

## 2.3. Single junction solar cell

A solar cell constructed from a-Si with either a single p-i-n or n-i-p junction is known as a single junction device. In Figure 2.9, you can see a schematic representation of this single junction solar cell, which is arranged in a superstrate configuration.

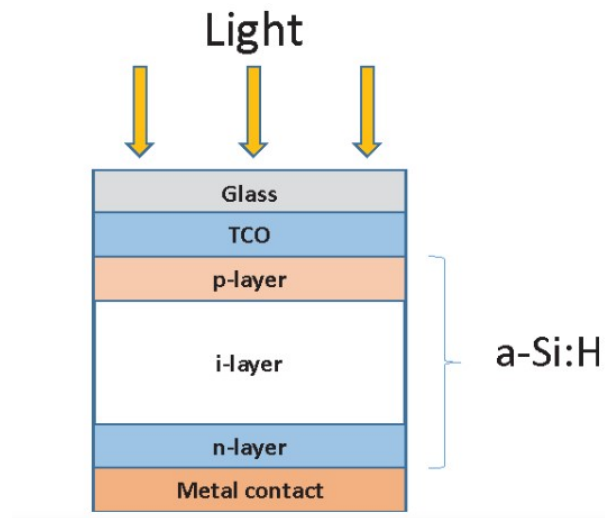


Figure 2.9: Architecture of single junction solar cell with superstrate p-i-n configuration [29].

These cells feature both p and n layers that generate an internal electric field across the intrinsic (i) layer composed of amorphous silicon. Given amorphous silicon's strong light absorption properties, the i-layer typically measures between 0.2 and 0.5 micrometers in thickness [22]. Amorphous silicon exhibits less structural consistency. As electrons and holes travel through the material, the chance of recombination increases over longer distances. To address this challenge, the i-layer must be precisely tuned in thickness—thick enough to absorb light effectively but not so thick that it impedes efficient conduction.[30]

In thin-film silicon solar cells, electrons move much more easily than holes [31]. To optimize hole collection, the P-doped layer is applied first as a window layer, ensuring that more holes are generated close to it. Additionally, a transparent conductive oxide (TCO) layer is positioned between the glass and the P layer to facilitate the lateral flow of charge carriers toward the electrodes. Most of the light absorption takes place in the intrinsic absorber layer, which is placed after the P layer. This is followed by a thin n-doped layer. The assembly is completed with a thin back reflector, made of zinc oxide or silicon oxide, and a metal back contact.

## 2.4. Multi-junction a-Si:H solar cells

Degradation in a-Si solar cells can be alleviated by using thinner intrinsic layers. These thinner layers produce a stronger internal electric field that resists distortions more effectively[32]. Nevertheless, the drawback is a reduction in light absorption. To maintain stability while preserving absorption efficiency, one effective approach is to stack several single-junction cells with thin intrinsic layers, a technique called the multi-junction concept. Additionally, this multi-junction setup enhances spectral utilization, as outlined in Figure 2.10.

When two junctions are layered on top of each other, the result is called a tandem or double-junction solar cell. A triple-junction solar cell, on the other hand, includes three such stacked junctions. Despite having multiple layers, the total thickness of a multi-junction solar cell is similar to that of a single-junction cell, though each layer is thinner and less likely to suffer from light-induced damage. Moreover, the multi-junction design enables each layer to be fine-tuned to absorb different parts of the solar spectrum, which broadens the range of light it can utilize and improves the cell's overall efficiency.

Multi-junction solar cells have a much more intricate structure compared to traditional single-junction cells. A key requirement for the effective operation of these multi-junction cells is the inclusion of a tunnel-recombination junction (TRJ) between the layers, which must have very low electrical and optical losses[33].

The initial requirement stems from the need for the individual cells to function as current sources arranged in series. Thus, it is crucial that each cell produces an identical current. The amount of current

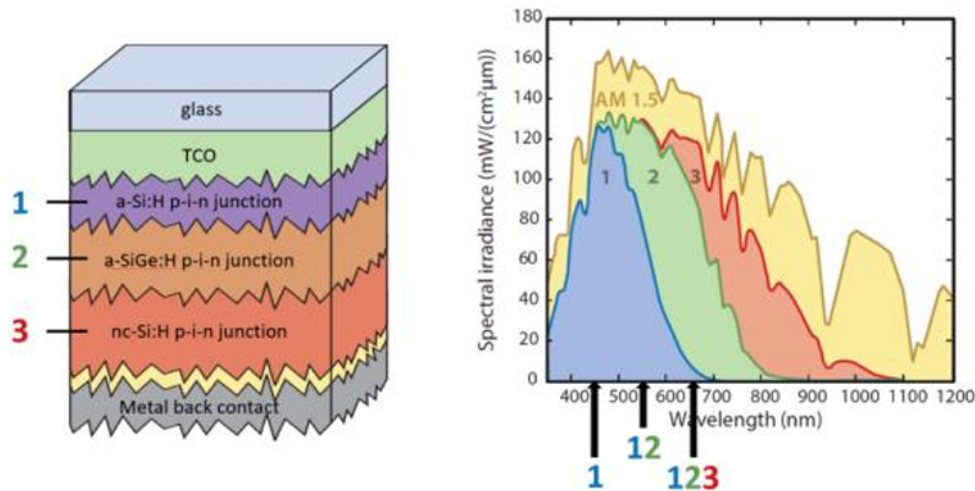


Figure 2.10: Spectral utilization of Multi-junction solar cell [15].

generated is mainly determined by the thickness of the intrinsic layer. To ensure consistent current output, the thickness of each intrinsic layer must be carefully calibrated to account for the distribution of photogenerated carriers, referred to as the generation profile.

The second requirement concerns the interface between the individual cells. This interface acts like an n-p diode and becomes reverse-biased when the cells are forward-biased. For optimal performance, an ohmic contact is needed instead of a rectifying one. This issue can be resolved by incorporating a tunnel-recombination junction (TRJ), which ensures that electrons from the n-type layer of the upper cell fully recombine with holes from the p-type layer of the lower cell at their interface. Such recombination is vital for maintaining current flow through the solar cell. The reverse-biased p-n junction creates a strong electric field that aids carrier tunneling to the defect states at the junction, where effective recombination takes place. Typically, achieving a TRJ involves using microcrystalline silicon in at least one of the doped layers or adding a thin oxide layer at the interface to increase defect density[34].

The Figure 2.11 illustrates the configuration of an a-Si:H/a-SiGe:H tandem cell. The a-Si component cell captures photons with energies greater than 1.70 eV, while photons with lower energies, which pass through the a-Si top cell, have an opportunity to be absorbed by the a-SiGe bottom cell.

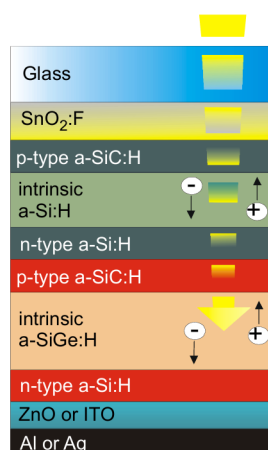


Figure 2.11: Device architecture of a-Si:H based multi-junction solar cell with superstrate p-i-n configuration [15].

## 2.5. Fabrication techniques

### 2.5.1. Plasma Enhanced Chemical Vapour Deposition (PECVD)

The silicon-based thin films were fabricated using plasma-enhanced chemical vapor deposition (PECVD). The Figure 2.12 provides a schematic representation of the PECVD apparatus. In PECVD, plasma is employed to activate the precursor gases. The process generally involves introducing a mixture of precursor gases into a vacuum chamber containing a substrate. Radiofrequency or microwave energy is then applied to generate plasma in the gas mixture, dissociating the precursor molecules into reactive species. These species then react and deposit onto the substrate, forming a thin film. Deposition parameters such as pressure, power, gas flow rate, and temperature can be adjusted to optimize the film's performance.

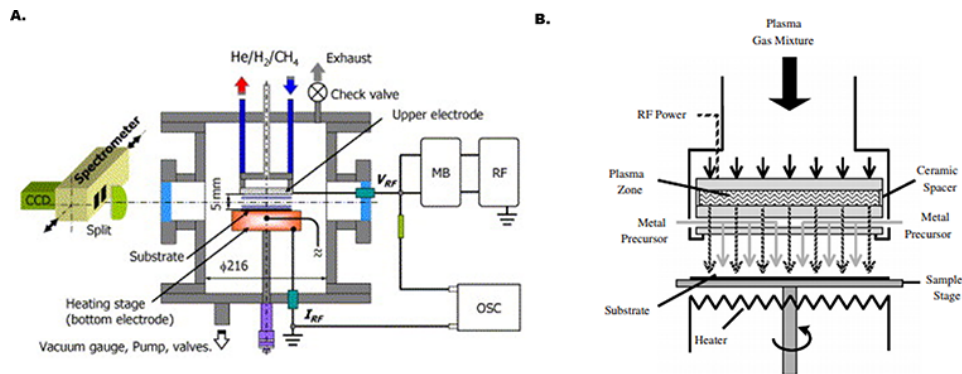


Figure 2.12: schematic representation of the PECVD [35].

The process of fabrication via PECVD needs to be carried out carefully. Firstly, the condition of the chamber needs to be carried out for around one hour. The Figure 2.13 indicates the control page in PECVD used in Tu-delft, the coating parameters like power, pressure, and gas flow rate can be settled. Moreover, the purge button is used before and after the fabrication to remove the gas remaining on the substrate. The pressure can be set and throttled on the page and this process normally takes 30 seconds to stable the pressure.

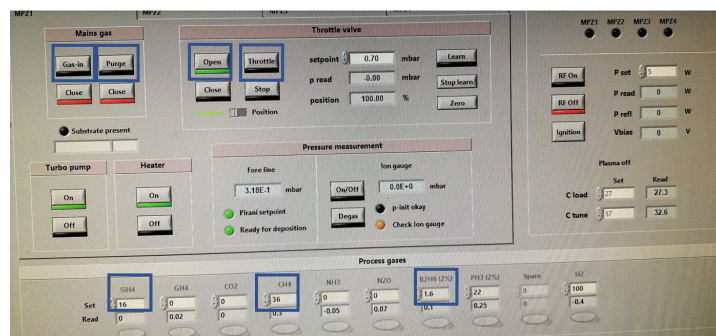


Figure 2.13: Control page of PECVD

To be mentioned, the reflection power should be minimized to obtain stable plasma generation, this can be achieved by turning the load position and tune position, and the reflected power can be seen on the monitor, which can be referred to in Figure 2.14.



Figure 2.14: Tuning of reflected power.

## 2.6. Characterization processes

In this section, the techniques required to characterize a fully fabricated solar cell are explained.

### 2.6.1. Current-voltage measurement

The JV measurement, or current-voltage measurement, is an essential method for assessing the performance of photovoltaic (PV) devices. This technique involves exposing the solar cell to light and recording its current output as the voltage is varied. This process enables the evaluation of important performance metrics.

To determine the external characteristics of a solar cell, current-voltage measurements are taken using the power and JV curves obtained. This process is carried out with a WACOM solar simulator, which uses both a xenon lamp and a halogen lamp. The xenon lamp is equipped with filters to remove strong infrared emission lines, providing a more accurate simulation of the solar spectrum. During these measurements, a standard solar irradiance of 1 Sun ( $1000 \text{ W/m}^2$ ) is applied.

The solar cell is placed on a stage with a liquid cooling system that keeps the temperature at  $25^\circ\text{C}$ . The setup is controlled by computer software, which immediately shows the JV curve along with key external parameters, including short-circuit current density ( $J_{sc}$ ), fill factor (FF), open-circuit voltage ( $V_{oc}$ ), series resistance ( $R_{sc}$ ), and shunt resistance ( $R_{oc}$ ).

### 2.6.2. External quantum efficiency measurement

External Quantum Efficiency (EQE) is an important metric for assessing solar cell performance. It gauges how effectively a solar cell converts incoming photons of a specific wavelength into charge carriers (electrons or holes). Essentially, EQE reflects the efficiency of converting incident light into electrical current. Presented as a percentage, EQE varies with wavelength, offering insights into the cell's response across different segments of the solar spectrum. A high EQE over a wide range of wavelengths suggests that the solar cell is both well-designed and efficient[36].

In Figure 2.15, a diagram of the EQE measurement setup is shown. The setup uses a light source that is filtered to emit only a single wavelength, making the light monochromatic. The solar cell being tested is exposed to this monochromatic light, which is varied across a spectrum typically ranging from ultraviolet (UV) to near-infrared (NIR). Before conducting the measurements, the light intensity is calibrated using either a photodiode or a reference solar cell with a known EQE. This calibration is crucial for ensuring precise measurement of the photon flux hitting the cell.[36]

The External Quantum Efficiency (EQE) of a multijunction solar cell is more involved than for single-junction cells because of the multiple layers present. This process generally requires dividing the light into various wavelength ranges to match the absorption properties of each junction. Additionally, bias light sources are used to correctly bias the other junctions while focusing on the EQE measurement of a specific sub-cell. For instance, when assessing the EQE of the bottom cell, the bias light should be set up to stimulate the upper cells without significantly influencing the performance of the bottom cell.

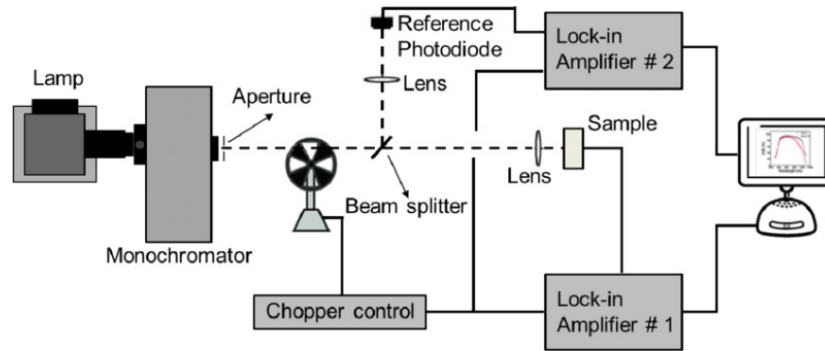


Figure 2.15: schematic representation of EQE measurement [37].

When testing multi-junction solar cells, exposing the top cell to short-wavelength monochromatic light can prevent the bottom cell from absorbing any light, resulting in no current from the tandem cell. To resolve this issue, we use bias illumination by shining light that the top cell does not absorb, such as infrared light, to saturate the bottom cell. This ensures that the current in the series-connected cells is controlled by the top cell, which is the intended outcome. Conversely, to measure the response of the bottom cell, we need to illuminate the top cell with short-wavelength light, such as blue or ultraviolet light. The EQE curves obtained from this method were for a micromorph tandem cell consisting of an amorphous silicon top cell and a microcrystalline silicon bottom cell.

### 2.6.3. Spectroscopic Ellipsometry

The Figure 2.16 presents a schematic of Spectroscopic ellipsometry (SE), an optical technique characterized by its non-destructive, non-contact, and non-invasive nature. This method relies on observing the change in the polarization state of light as it obliquely reflects off a thin film sample. Spectroscopic ellipsometry employs a model-based approach to determine the optical properties.

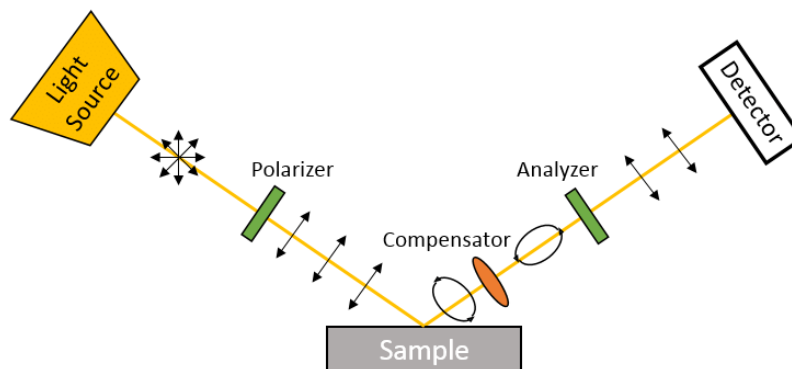


Figure 2.16: schematic representation of Spectroscopic Ellipsometry [38].

The measured polarization change due to reflection at the sample is fitted using an optical model that represents the film or stack of films which can be referred to Figure 2.17. The mean square error (MSE) represents how to match the model and the measurement. Fitting aims to minimize the mismatch between the measurement and the model. This can be achieved by referring to the waveform which shows the bottom side of Figure 2.17. The y-axis is the psi which represents the amplitude ratio of the p- and s-polarized light waves after reflection from a sample surface, and the x-axis represents the wavelength. The general process to minimize the MSE is to make the thickness value match how many peaks of the waveform. More peaks of the waveform represent the thicker of the material. In this case, the two peaks of the waveform can be seen in Figure 2.17 which represents the thickness of range between 100nm to 200nm. After adjusting the value of thickness, normally the EMS can be reduced

dramatically. The next step is to adjust the energy band gap of Eg1 until the MSE is smaller. In general, the MSE under 10 is considered a good fit between the model and the measurement.

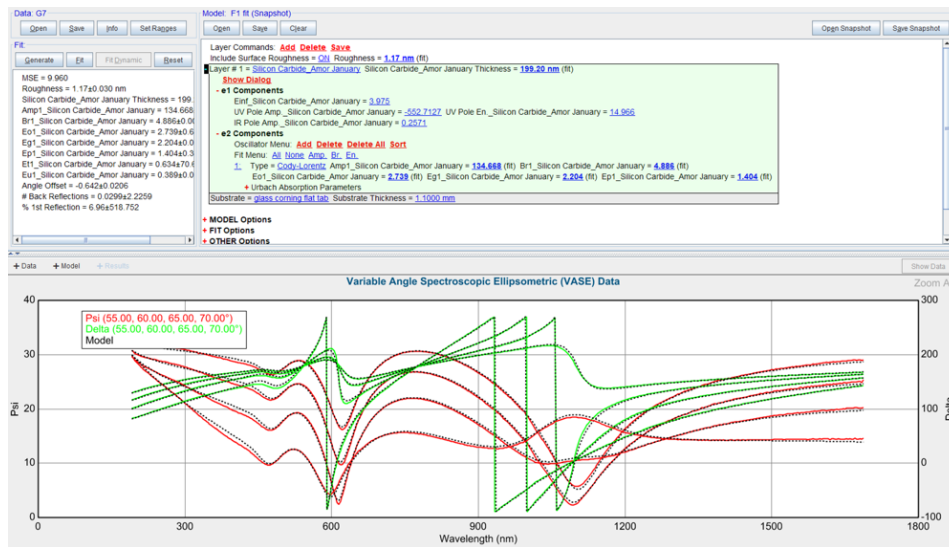


Figure 2.17: The model of Spectroscopic Ellipsometry

To accurately extract valuable details like film thickness and optical properties, it's essential to model the near-surface region of the sample and fit the spectroscopic ellipsometry (SE) data to this model, treating the relevant parameters as variables during the numerical analysis. The precision of this analysis is crucial, as incorrect modeling of the SE data can result in misleading or useless outcomes. [39]

#### 2.6.4. Dark conductivity

Dark current is the current flowing through a detector when no photons are incident. This measurement is essential for determining the baseline current that must be exceeded by photocurrent for a material to be considered photoactive. Additionally, analyzing how dark current varies with temperature can provide insights into the activation energy ( $E_a$ ), which represents the height of the potential barrier between different energy states. Lower activation energy is generally desirable for higher conductivity. The setup for performing dark JV measurements is depicted in Figure 2.18.

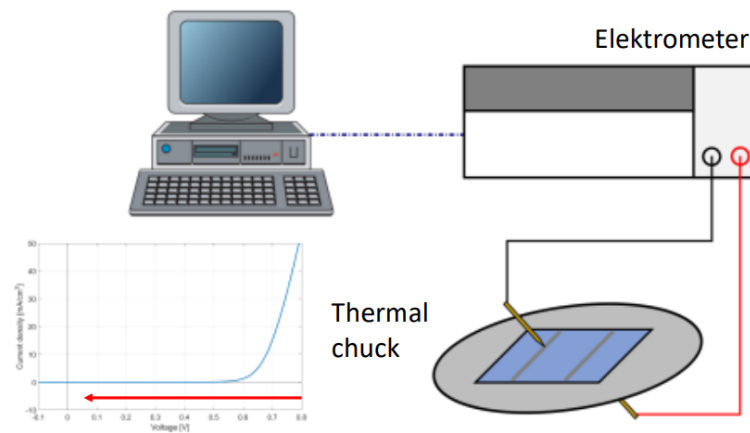


Figure 2.18: Schematic representation of dark conductivity [40].

### **2.6.5. Reflectance measurement**

The Perkin-Elmer spectrometer is an advanced tool designed to analyze how light interacts with materials. It determines the composition and concentration of substances by measuring their light absorption, emission, or scattering, particularly for reflectance studies. The system features mirrors, lenses, and filters to manage the light paths. Two beams of monochromatic light are used—one for testing and the other for reference. Light is provided by tungsten halogen and deuterium lamps, covering a range from 175 nm to 3300 nm.

The integrating sphere, lined with Spectralon (a material known for its scattering and reflectivity), is where the monochromatic beams converge. Light within the sphere undergoes multiple reflections and scattering, ensuring precise measurement of light intensities due to the uniform electromagnetic field. Two types of detectors capture light intensity at various wavelengths. During measurement, three key values are recorded: reflectance (R), transmittance (T), and absorptance (A). As light interacts with the solar cell, it is either reflected, absorbed, or transmitted through the cell.

# The fabrication of Boron doped Silicon Carbide with PECVD

## 3.1. Introduction

Boron-doped Silicon carbide (SiC) is conventionally used for the p-layer in thin-film silicon solar cells. Boron-doped silicon oxide is another option to be used as a front p layer for a solar cell. It has an advantage over silicon carbide due to its transparency. The previous study done at TU Delft for LID on amorphous silicon single junction solar cells with boron-doped nanocrystalline silicon oxide as a p-doped layer has shown a significant degradation under light [41]. As a result, a systematic study to compare the two is performed in this work. Before that investigation is carried out, the p-doped silicon carbide layer itself needs to be optimized. This chapter studies the optimization of the recipe for boron doping of silicon carbide layers that can result in comparable results in amorphous single junction solar cells.

The Figure 3.2 presents the EQE comparison between p-a-SiC and p-nc-SiO<sub>x</sub>, it is clearly to be seen that the overall EQE performance of p-a-SiC suffers from the reflection and low diffusion length and significantly affected by parasitic absorption in the short wavelength range.

Furthermore, the Figure 3.3 is the JV curve between p-a-SiC and p-nc-SiO<sub>x</sub> before optimization. It can be seen that the p-a-SiC suffers from the band gap misalignment, resulting in an S-shaped curve (Red curve). As a result, the optimization of fabrication of the p-SiC layer is required to be carried out before investigating the light-induced degradation.

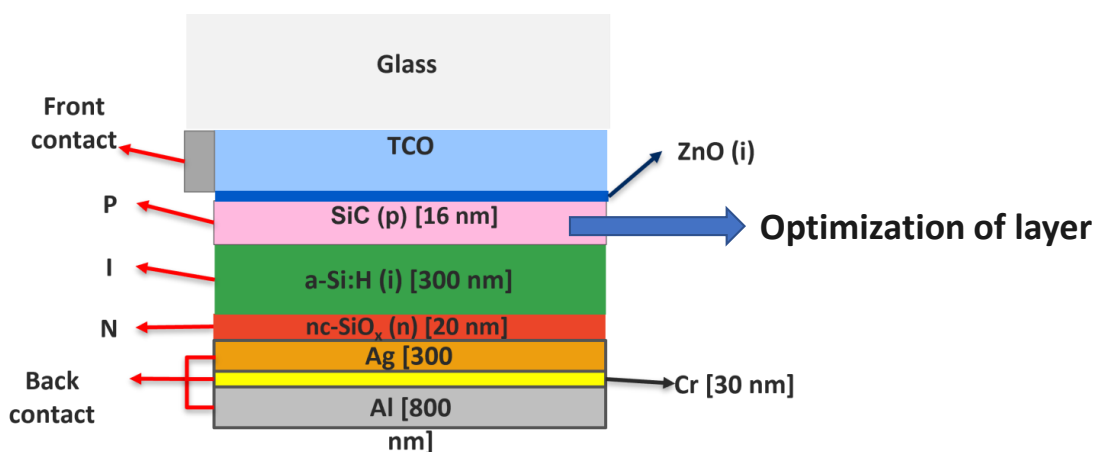


Figure 3.1: Optimisation of P doped silicon carbide layer for superstrate configuration

In this chapter, p-doped SiC deposition conditions for a Plasma-enhanced chemical vapor deposition (PECVD) is optimized. The cell architecture with p-a-SiC window layer in PIN configuration is

illustrated in Figure 3.1. The characterization is performed using Spectroscopic ellipsometry (SE) and dark conductivity measurements.

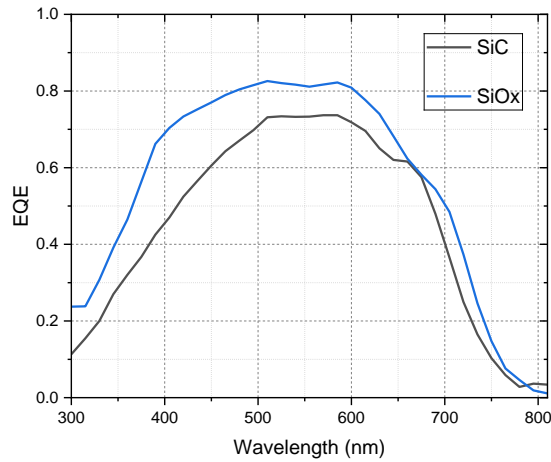


Figure 3.2: EQE comparison between p-a-SiC and p-nc-SiOx

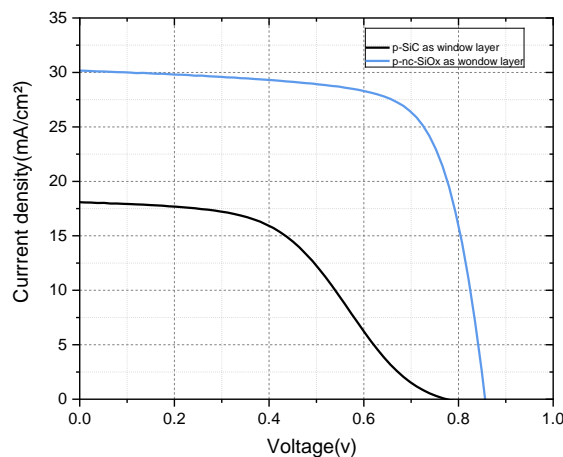


Figure 3.3: JV curve between SiC and SiOx before optimization

## 3.2. Background study

This section provides a concise summary of the existing background information on the application of silicon carbide and silicon oxide in multi-junction solar cells, as well as an overview of the principles of plasma-enhanced chemical vapor deposition (PECVD).

### 3.2.1. SiC and SiOx

Silicon carbide (SiC) offers several benefits for solar cells, including superior thermal stability, a broad band gap, and a high electric breakdown field[42]. Despite these advantages, SiC solar cells can suffer from light-induced degradation, which affects their efficiency. When exposed to light, defects can form within the material. These defects act as centers for recombination, reducing the lifespan of charge carriers and thereby diminishing the cell's overall efficiency[43].

To mitigate the effects of light-induced degradation, researchers have investigated various passivating layers for SiC solar cells, such as amorphous silicon carbide (a-SiC). The use of a-SiC passivating layers

has been shown to improve the performance of SiC solar cells by reducing the density of surface states and hence the recombination rate. Hydrogenated amorphous silicon oxide (a-SiO<sub>x</sub>:H) films have been used for solar cell fabrication, as their characteristics are suitable for wide band gap top cells of a multi-junction solar cell[44].

Few of the important properties of the p-type layer that influence the blue response of the cell are high conductivity, low thickness, high optical band gap, low defect density, etc.

### 3.2.2. PECVD

The existing PECVD system was automated to streamline operations and establish a recipe-driven process for creating thin-film silicon devices. This precise control over deposition parameters allows for the production of intricate device structures with minimal reliance on the operator's expertise, as shown by the samples created using the system. The next phase involves analyzing various samples made under specific conditions to identify the optimal parameters for the system. This will facilitate the group's research into electronic sensors by enabling the production of sophisticated multilayer electronic devices.[45].

## 3.3. Methodology

This section outlines the methodology used to investigate the fabrication of P-SiC via PECVD. The process for investigating the deposition parameters is illustrated in the design of the experiments.

### 3.3.1. Film deposition

The p-doping layer on SiC solar cells is deposited onto Corning glass Xa. Each sample has the p-layer applied for a duration of 20 minutes. The deposition rate is determined through spectroscopic ellipsometry (SE) measurements. High-frequency power at 13.56 MHz is employed to enhance power conversion efficiency and to consume less energy compared to lower-frequency alternatives in the PECVD process. The chamber is conducted at 300 degrees Celsius. The Figure 3.4 illustrates the process of fabrication and characterization for the P layer. It can be seen that the first step is to investigate the different coating parameters like power, pressure, and gas flow rate. Three gas sources for fabricating the P-doping silicon carbide are silane, methane, and diborane. After fabricating the P-SiC in PECVD, the dark conductivity measurement is carried out to get the electrical properties like dark conductivity and activation energy. The samples are required to do the annealing at 130 degrees Celsius for 30 minutes before measuring dark conductivity to get better conductivity.

Finally, the Spectroscopic ellipsometry (SE) measurement is carried out to obtain the optical properties like energy band gap, refractive index, and absorption coefficient. Also, the dark conductivity measurement is carried out to obtain the conductivity and activation energy.

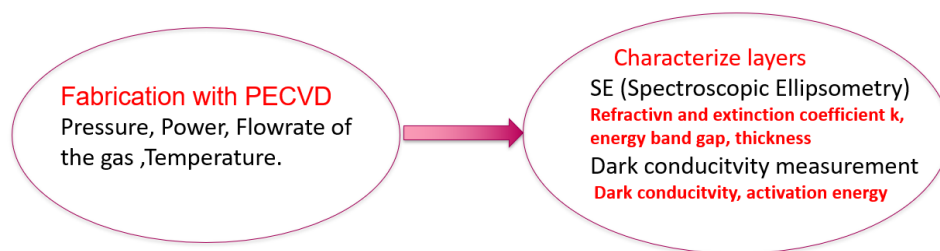


Figure 3.4: The process of fabrication and characterization for P layer

### 3.3.2. Design of experiments

The object is to optimize the fabrication of p-a-SiC to derive better optical and electrical performance. The power, pressure, temperature, and flow rate of gas are turned to optimize the layer, and silane (SiH<sub>4</sub>), methane(CH<sub>4</sub>), and diborane B<sub>2</sub>H<sub>6</sub> are used as the gas source for p-SiC. The overall process of experiment can be seen in Figure 3.5

In terms of PECVD, the power, and pressure is selected as the first two investigated deposition parameters, the starting point is at 5W and 0.7 mbar, and go into different directions to see the optimal zone, and once

the optimal direction is found, the more detail investigated in which deposition parameters combination between power and gas is the good one. In the second round, the different gas flows of B<sub>2</sub>H<sub>6</sub> are selected to see whether the concentration of boron will affect the performance of p-a-SiC. In the third round, the gas flow of CH<sub>4</sub> is investigated to see whether the concentration of C will affect the performance of p-a-SiC. This experiment aims to fabricate good performance of p-SiC with a high energy band gap and high conductivity.

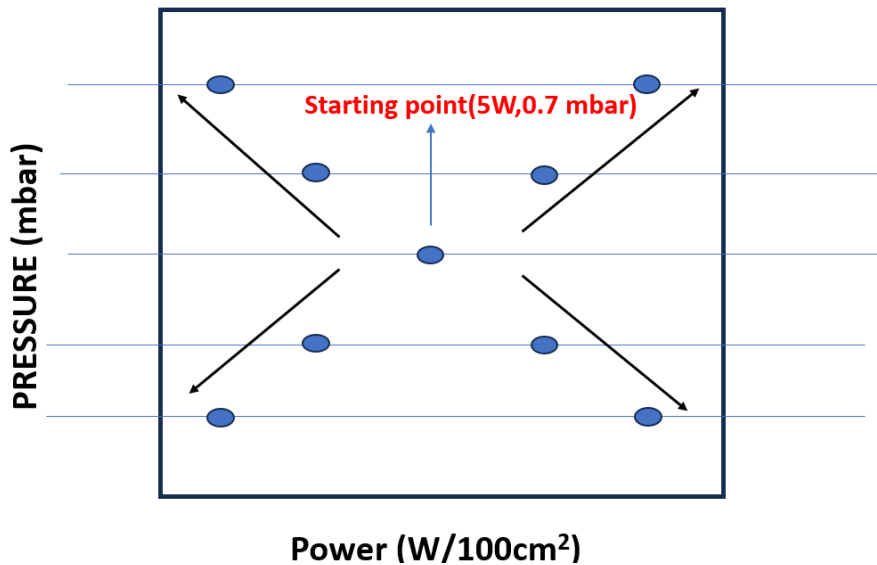


Figure 3.5: Design of experiment

## 3.4. Results and Discussion

### 3.4.1. Optical and electrical performance

#### Activation energy:

The activation energy in a semiconductor refers to the minimum energy required for charge carriers (electrons or holes) to move from one energy level to another, enabling electrical conduction. In general, doped layers based on wide band gap materials will have beneficial band bending when the activation energy is lower resulting in high cell performance. Also doping generally reduces the activation energy required for charge carriers (electrons or holes) to move into the conduction or valence bands. This makes it easier for electrical conduction to occur. In this experiment, the activation energy was measured with the dark conductivity measurement based on the different coating parameters which can be seen in Figure 3.6. The trend can be seen that the higher the deposition power the lower the activation energy. This is because higher power can dissociate more B<sub>2</sub>H<sub>6</sub>, which makes the activation energy lower. The Fermi level is closer to the valence band[46].

In terms of pressure, the higher pressure leads to the lower activation energy. This is due to the high pressure representing more particles inside the chamber which causes an increase in the residence time of B<sub>2</sub>H<sub>6</sub> precursor gas allowing based on the handbook of PECVD[47], more B<sub>2</sub>H<sub>6</sub> to be dissociated. This might lead to more boron incorporation and a reduction in activation energy[48].

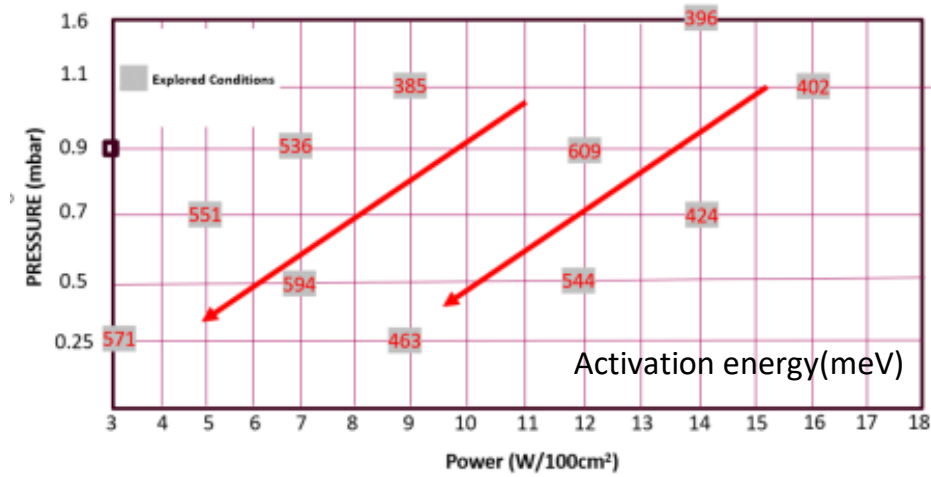


Figure 3.6: Activation energy in different power and pressure

In the experiment of power and pressure variation, the processing condition resulting in the lowest activation energy, at 9W and 1.1 mbar respectively, has been selected. In the next experiment, the B<sub>2</sub>H<sub>6</sub> flow and CH<sub>4</sub> flow have been varied. It can be seen in the Figure 3.7 that the higher the gas flow of B<sub>2</sub>H<sub>6</sub>, the lower the activation energy, due to more boron incorporation into the layer.[49]

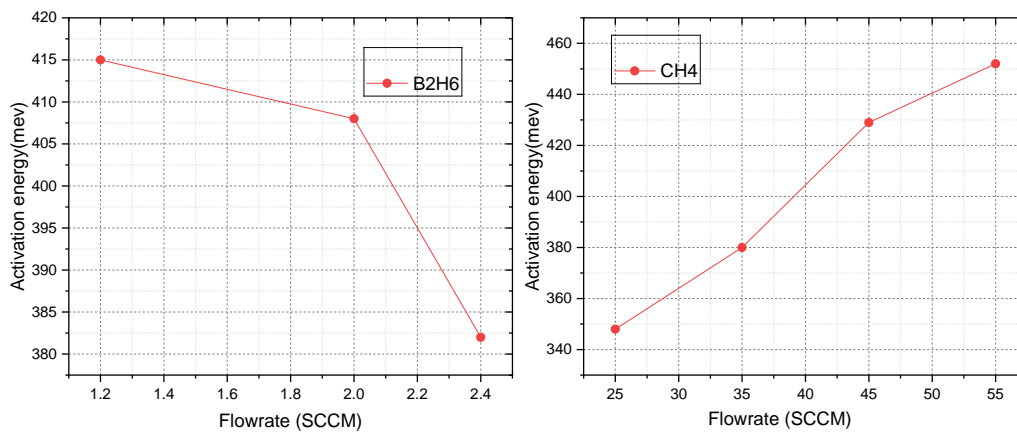


Figure 3.7: Activation energy in different gas flow rate of diborane(B<sub>2</sub>H<sub>6</sub>) and methane(CH<sub>4</sub>)

Moreover, the activation energy changes with the increase of CH<sub>4</sub> can be referred to in Figure 3.7, it can be seen that activation increases with the increase of CH<sub>4</sub>. This increase the energy band gap. This leads to the increase of activation energy as well[50].

### Dark conductivity

Dark conductivity in semiconductors provides information about the intrinsic electrical properties of the material and influences the performance of electronic and optoelectronic devices. The higher dark conductivity is targeted in this experiment. Figure 3.8 shows that higher pressure and lower power results in higher dark conductivity.

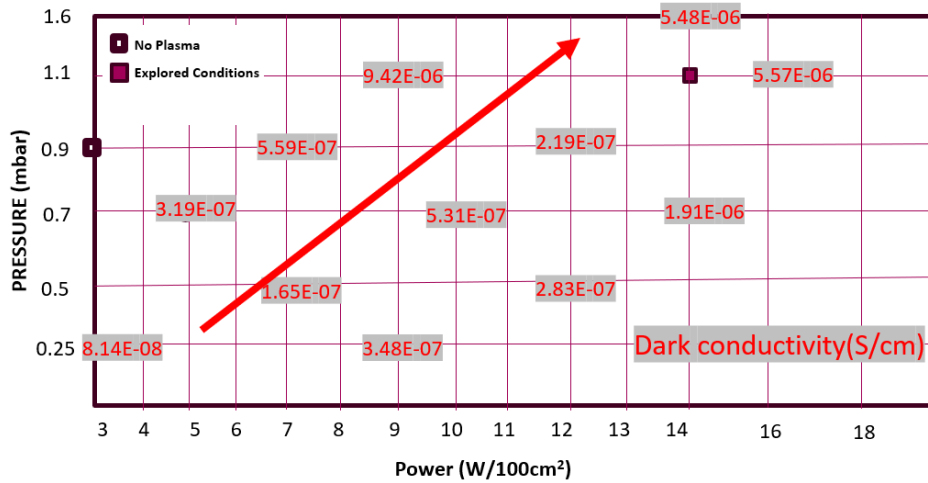


Figure 3.8: Dark conductivity in different power and pressure

The relation between B2H6 and CH4 gas flow is presented in Figure 3.9. The dark conductivity increases with increasing B2H6 flow and decreasing CH4 flow. This is in line with the trends for activation energy observed in Figure 3.7.

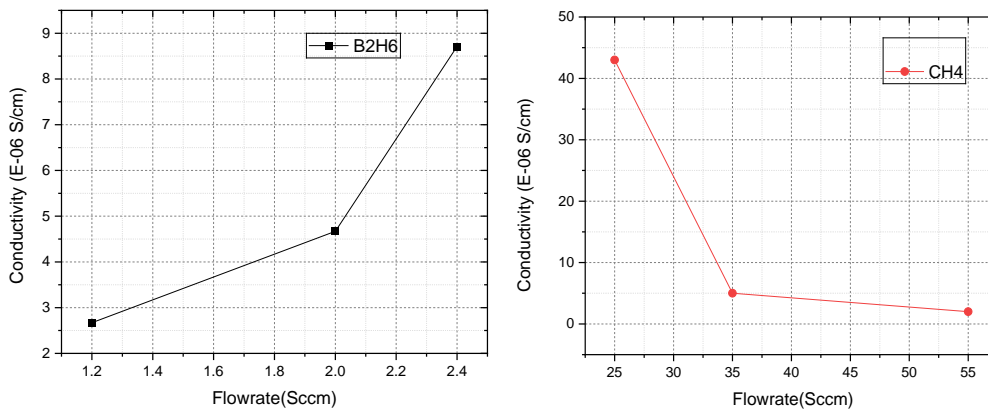


Figure 3.9: Dark conductivity in different gas flow rate of diborane(B2H6) and methane(CH4)

**Energy band gap(EG1)**

The energy band gap represents the minimum energy required to excite an electron in a semiconductor to a higher energy state. Only photons with energy greater than or equal to a material’s band gap can be absorbed. Ideally, the larger energy band gap is preferred to absorb more light, and applying the silicon carbide is also for this purpose. In terms of coating parameters for contributing to the higher energy band gap, first of all, based on the Figure 3.10, which indicates that an increase of power or increase of pressure increases the energy band gap. Based on the research of [51], when the amount of atomic silicon is available for film growth it leads to crystallization. In other words, if more silicon dissociates in the substrate than carbon does during the fabrication when the increase of power and pressure, the energy band gap will be reduced. This is due to the film with more silicon having a lower energy band gap compared to the film with more carbon content[52], the similar concept also can be seen in Figure 3.11.

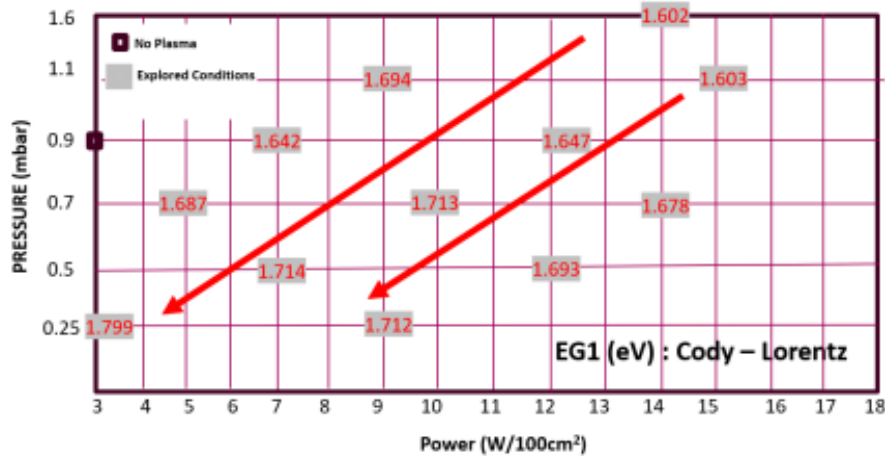


Figure 3.10: Energyband gap in power and pressure

The Figure 3.11 indicates that the increase of B2H6 does not change the bandgap energy, it only affects the activation and dark conductivity.

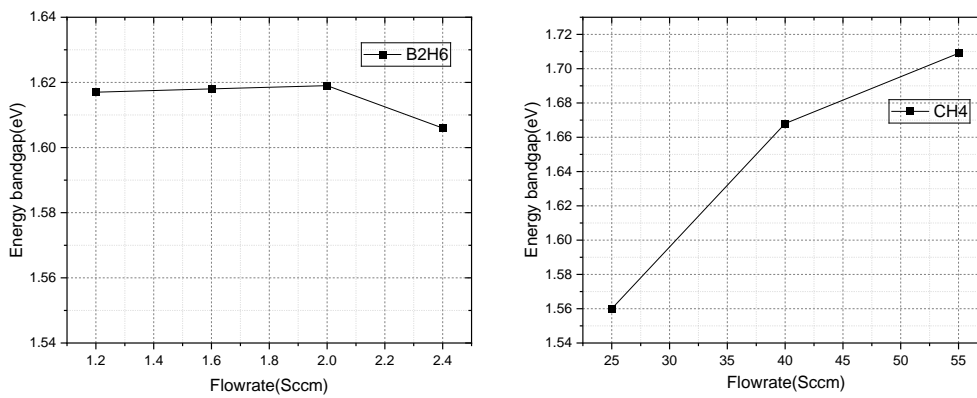


Figure 3.11: Energy bandgap in different gas flow rate of diborane(B2H6) and methane(CH4)

As the methane flow increases, so does the film’s carbon content. This means that the band gap tends towards that of a carbon thin film, which is higher than the band gap of amorphous silicon thin films. This, explains the increase in the band gap proportional to carbon content. Similar results can be seen in Figure 3.11. However, the increase in carbon also leads to an increase in activation energy.

**Refractive index**

The refractive index of an optical medium is a dimensionless number that gives an indication of the light-bending in that medium. The refractive index is wavelength and material-dependent. The Figure 3.12 is the refractive index of different combinations of power and pressure at wavelength 900 nm. Based on the experiment of [53], for a typical P-SiC fabricated with PECVD, For a typical sample of SiC the refractive index at 632.8 nm is 2.6353. It can be seen in Figure 3.12 that the higher the power input, the lower is the Refractive index. This is due to the faster dissociation of precursor gases resulting in optically less dense substrate. Also, a decrease in pressure which in turn results in slower deposition and denser materials causes a high refractive index material.

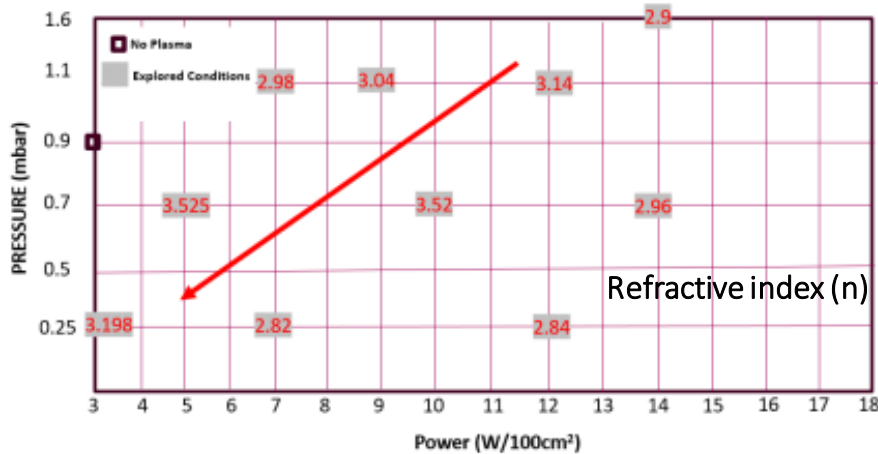


Figure 3.12: Refractive index in different power and pressure combinations at wavelength 900nm

### 3.5. Results of optimization of p-SiC

#### EQE characterisation

After optimization of p-SiC by PECVD techniques, the improvement in EQE is shown in Figure 3.13. The black line, corresponding to solar cells before p-layer optimization, shows an EQE that suffers from parasitic absorption. In contrast, the red EQE representing the solar cell with the optimized layer performs better overall wavelengths. The optimal receipt of making the p-SiC is at 9W, 1.1 mbar, SiH<sub>4</sub> 16 sccm, CH<sub>4</sub> 50 sccm, B<sub>2</sub>H<sub>6</sub> 15 sccm.

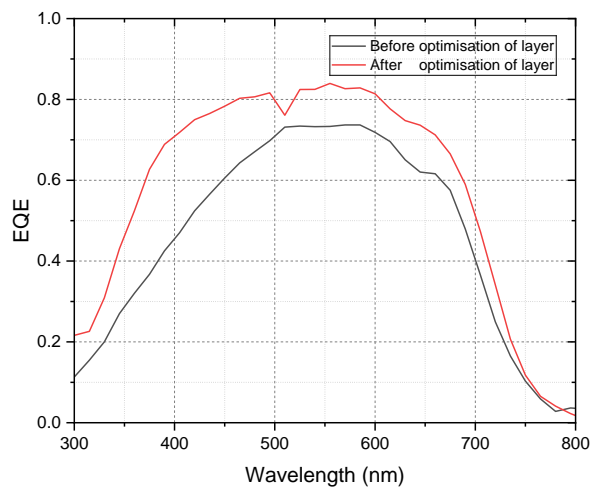


Figure 3.13: EQE of p-i-n solar cell including the p-a-SiC layer before and after optimization of fabrication

#### Illuminated JV characterisation

After optimization of P-SiC via PECVD, the performance of JV curve before and after optimization can be seen in the Figure 3.14. It can be clearly seen that the performance of JV before optimization includes an energy barrier shown by the S-shaped curves. This normally indicates an issue with charge carrier transport between the layers of your device. In contrast, the red JV curve represents the optimized layer which has also solved the energy band gap mismatch.

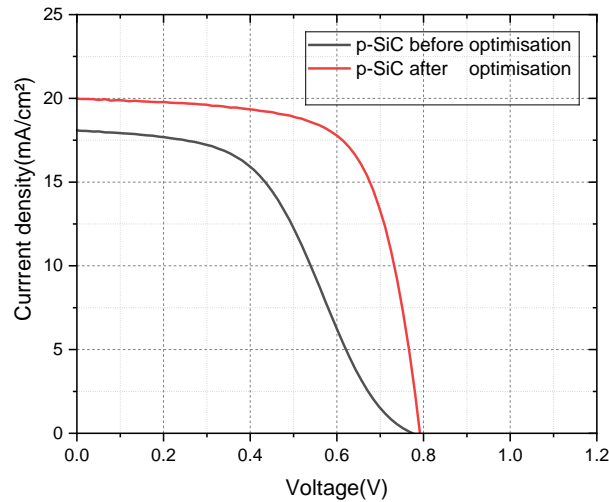


Figure 3.14: JV curve before and after optimization

### 3.6. Discussion

The results of JV and EQE measurement show that the not-optimized fabrication of the P doping layer leads to significant parasitic absorption, and the poor EQE performance. Furthermore, the cell with an energy barrier has a low fill factor and an S shape of JV curve. To optimize the fabrication of p-SiC, coating parameters like power, pressure, and gas flow rate need to be investigated in PECVD to obtain good electrical and optical performance.

Based on the results of the characterization from dark conductivity and spectroscopic ellipsometry measurement, some trends can be observed. First of all, an increase in the power and pressure will increase the deposition rate, lower the activation energy, higher the conductivity, and decrease the energy bandgap. Secondly, the increase of gas flow rate in diborane leads to a higher concentration of boron dissociated in the substrate, which lowers the activation energy and higher the conductivity. Finally, the increase of gas flow rate in methane leads to a higher concentration of carbon, which higher the energy band gap but also increases the activation energy. This is due to the more degrees of sp<sup>3</sup> bonding formed when more carbon context increases[54].

Furthermore, to overcome the energy barrier in devices, one approach is to dope the transport layers, which enhances the alignment of energy levels between the P-layer and the absorption layer. [55]. This doping increases the conductivity of the charge transport layers.[56]. Additionally, incorporating a passivation layer into the charge transport or adjacent layers can help regulate charge flow within the device[57].

In summary, the deposition parameters have an interdependent effect on the performance, and the optimal combination for fabrication of the p-SiC are at the processing conditions of Power 9W, pressure 1.1(mbar), SiH<sub>4</sub>: 16(sccm), CH<sub>4</sub>: 50(sccm), B<sub>2</sub>H<sub>6</sub>:15 (sccm) in this experiment.

# 4

## LID study of Different Solar cell Architectures

### 4.1. Introduction

One significant drawback of amorphous silicon solar cells is their susceptibility to light-induced degradation (LID) when exposed to light [2]. This phenomenon, known as the Staebler-Wronski effect, impairs efficiency by causing the breakdown of fragile silicon-hydrogen bonds within the absorbing layer, which in turn increases the number of defects. The extent of this effect is highly influenced by factors such as the quality and thickness of the intrinsic a-Si layer, operational temperature, light intensity, and other conditions[58]. The standard test for the LID uses an illumination of 1000 W/m<sup>2</sup> at 50°C for 1000 hours at open circuit conditions, which is different from the real-life operation of the solar cells.

As discussed in Chapter 3, optimization of the p-sic benefits reduces the parasitic absorption. Following the optimization of the fabrication process for p-a-SiC using plasma-enhanced chemical vapor deposition (PECVD), it is necessary to conduct light absorption experiments to evaluate its degradation performance. This performance will also be compared to the degradation characteristics observed in the application of p-nc-SiO<sub>x</sub>.

Furthermore, to further confirm whether light induced degradation occurred in p-nc-SiO<sub>x</sub> is mainly at high energy wavelength. The bi-layer TCO (hydrogen-doped indium oxide (IOH) and intrinsic zinc oxide (i-ZnO) ) is investigated in the application of p-nc-SiO<sub>x</sub> window layer in the nanocrystalline solar cell to check whether light induces degradation still occurs when blue light is mainly absorbed in the intrinsic zinc oxide (i-ZnO) layer. Lastly, the LID of three micromorph tandem solar cells with different thicknesses of the intrinsic layer is investigated to see how to achieve better performance and degradation via the Current Matching method.

The cell characterization involves JV measurements and EQE measurements, which are used to determine various performance metrics such as fill factor (FF), open-circuit voltage (Voc), efficiency, short-circuit current density (Jsc), series resistance (Rs), shunt resistance (Rsh), and external quantum efficiency (EQE).

### 4.2. Background study

Even though considerable research has been dedicated to the Staebler-Wronski effect (SWE), its exact nature and underlying causes are still not fully understood. Nanocrystalline silicon shows reduced sensitivity to the SWE relative to amorphous silicon, suggesting that the disordered structure of amorphous silicon plays a major role in this phenomenon. Factors such as hydrogen concentration, its intricate bonding interactions, and impurity levels may also affect the SWE. This section summarizes the progress made in elucidating the SWE up to this point.

### 4.2.1. Proposed theories on SWE

Numerous theories offer explanations at the atomic level. During light soaking, the recombination of charge carriers induces structural defects, forming electronic states near the mid-gap. These states act as recombination centers, hindering the efficient collection of charge.

The **Density of Dangling Bonds** depicts the changes in the total density of light-induced degradation (LID) of dangling bonds in standard a-Si. The graph shows that the density of these dangling bonds rises with prolonged light exposure. Saturation of defect density occurs due to a balance between the creation and annealing of LID, regulated by hydrogen motion. The densities of dangling bonds (DBs) fluctuate over time until they eventually stabilize[59].

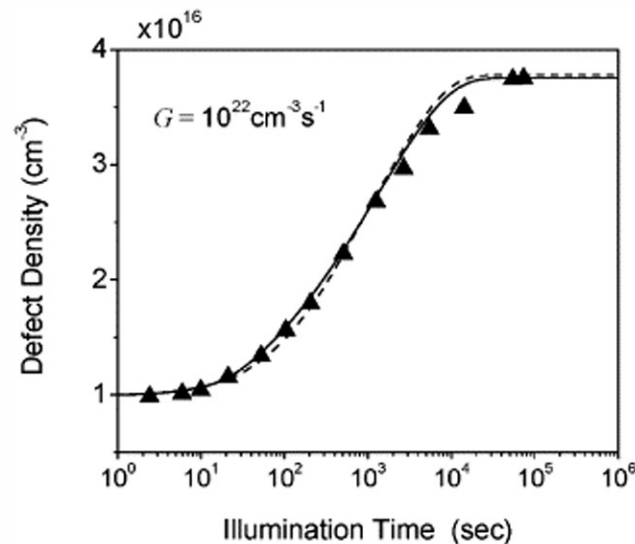


Figure 4.1: The density of dangling bonds with the function of light absorption time [59].

In 1985, Stutzmann, Jackson, and Tsai introduced the weak-bond model to elucidate the Staebler-Wronski effect (SWE) seen in hydrogenated amorphous silicon (a-Si). This model offers a theoretical perspective on the degradation caused by light exposure, which hampers the efficiency of a-Si solar cells [60]. According to the model, the weakening of certain bonds generates additional defect states, leading to shorter carrier lifetimes and higher recombination rates, thus lowering the cell's performance. The model also accounts for the partial reversibility of the SWE through thermal annealing, which helps reform Si-Si bonds and redistribute hydrogen, thereby lessening the number of dangling bonds. Nevertheless, the model faced criticism as it did not fully align with electron-spin resonance (ESR) data. For instance, localized phenomena like hydrogen migration near dangling bonds, which should have been detected by ESR, were not observed.

In 1999, Branz introduced the hydrogen collision model (HCM) to offer a different perspective on the Staebler-Wronski effect (SWE) in amorphous silicon (a-Si). This model highlights hydrogen's influence on defect formation and repair within the a-Si structure [61]. Unlike earlier models, the HCM addresses the absence of changes in ESR signals by emphasizing that hydrogen movement is a key factor, potentially more impactful than initially recognized. Hydrogen's localized hopping around dangling bonds might not generate a detectable ESR signal. The model integrates thermodynamic stability and kinetic factors related to hydrogen movement, aligning with the observed rates of defect formation and repair under varying conditions. By focusing on how hydrogen interacts with silicon, the HCM offers a broader view of the SWE, shifting the emphasis from just the silicon network's structure to the dynamics of hydrogen in the system.

The Figure 4.2 illustrates the process through a schematic configuration-coordinate diagram. According to this model, the recombination of excess charge carriers generates mobile hydrogen atoms (H<sub>m</sub>) and dangling bonds (DBs). Under normal conditions, these mobile hydrogen atoms tend to reattach to dangling bonds, preventing the formation of new dangling bonds. However, the Staebler-Wronski

effect can arise from occasional collisions between hydrogen atoms. When two mobile hydrogen atoms collide, they can form a metastable complex with two Si-H bonds, resulting in two metastable dangling bonds. The H collision model offers a fresh viewpoint on metastability by highlighting mobile hydrogen as a key precursor. The critical factor in determining the rate of metastable degradation is the density ( $N_m$ ) of mobile hydrogen. Due to the typically low density of  $N_m$  that causes degradation, detecting this phenomenon through spectroscopy is challenging, and further research is needed to clarify the connection between the Staebler-Wronski effect and the density of mobile hydrogen.

The intricate nature of the nanostructure made it challenging to accurately characterize the defects in a-Si [23]. Historically, the nanostructure of a-Si has been represented as a continuous random network (CRN) [62], where the primary defects are isolated dangling bonds. However, advancements in Fourier transform photocurrent spectroscopy have led to the view that a disordered network featuring hydrogenated vacancies (DNHV) offers a more precise depiction of the nanostructure in a-Si. Additionally, research using Fourier transform photocurrent spectroscopy indicates that defects associated with inadequately passivated vacancies and tiny voids are likely to be crucial in shaping the a-Si structure.

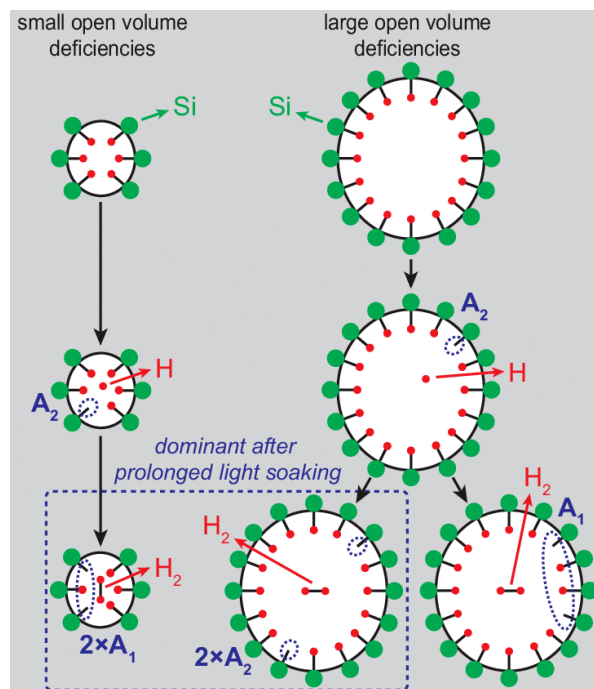


**Figure 4.2:** Schematic representation of a new nanoscopic model of the LID in a-si:H[60].

Melskens et al. [60] conducts an in-depth analysis of a-Si, emphasizing its nanostructures and defect characteristics. The study thoroughly explores how these factors impact the functionality of a-Si in different applications, with a particular focus on thin-film solar cells.

Hydrogen atoms are utilized to address dangling bonds—unpaired electrons on silicon atoms that can cause defects. Melskens investigates how these dangling bonds and the distribution of hydrogen atoms affect the electronic properties of the material. In addition, Melskens examines the local atomic arrangements within a-Si and finds that, even though the material is generally disordered, it features regions with more ordered structures called "Si-Si clusters." These clusters play a role in shaping the material's electronic behavior and its response to light.

In the context of light-induced degradation (LID), specific physical interpretations have been given to defects A1 and A2 at the nanoscopic level. Defect A1 is characterized by significant structural gaps or deficiencies within the amorphous silicon (a-Si) matrix. These gaps, which are essentially large vacancies or voids in the atomic arrangement, result in considerable open spaces within the material, often described as large cavities or open volumes within the silicon lattice.

Conversely, Defect A2 features smaller, more randomly scattered imperfections throughout the a-Si matrix. Unlike the large, open-volume voids seen with Defect A1, these A2 defects are spread more irregularly and affect the material in a different manner. As light-induced degradation (LID) progresses,

the quantity of these dispersed defects grows markedly. The size of these defects, denoted by  $S$ , shows a significant relationship with the length of light exposure.[63].

#### 4.2.2. Deposition Conditions and Their Impact on LID

The performance and stability of a-Si thin-film solar cells are significantly influenced by the deposition parameters and conditions. Light-induced degradation (LID) predominantly affects the intrinsic absorption layer. Numerous studies have highlighted how variations in thickness and hydrogen dilution impact the extent of LID in these solar cells. [64]

To start with, an increase in the thickness of the intrinsic layer results in more significant light-induced degradation of the cell. This occurs because a thicker intrinsic layer absorbs more light, generating a higher number of charge carriers. As these carriers recombine while the cell is illuminated, the defects and broken bonds also increase with the thickness, amplifying the Staebler-Wronski Effect.

Oppedal et al. [65] noted that changes in the thickness of the intrinsic layer have a lesser impact on the degradation of fill factor (FF) and open-circuit voltage ( $V_{oc}$ ) compared to short-circuit current density ( $J_{sc}$ ). Thinner intrinsic layers exhibit more abrupt band bending at the p-i and i-n interfaces, which generates a stronger electric field across the layer. On the other hand, thicker layers lead to more gradual band bending and a weaker electric field. Essentially, the sharp band bending in thinner layers results in a stronger electric field that aids in the efficient separation of charge carriers. As a result, the degradation of FF and  $V_{oc}$  due to light exposure is less severe because the enhanced electric field mitigates the increase in recombination losses.

Experimental data shows that the short-circuit current density ( $J_{sc}$ ) behaves differently depending on the thickness of the layer. Specifically, when the thickness surpasses 300 nm, there is a notable decrease in performance compared to the situation when the thickness is precisely 300 nm.[65]. The ratio of hydrogen dilution has a significant impact on both the microstructure and electronic characteristics of the film. By lowering the density of dangling bonds and enhancing the film's stability, hydrogen plays a crucial role. This highlights the importance of adjusting the hydrogen-to-silicon ratio to achieve high-quality amorphous silicon films.[64].

#### 4.2.3. Effects of Thermal Annealing

Thermal annealing involves heating a sample to a range of temperatures (200°C to 300°C) for a set period. For a-Si, this treatment is effective in reducing the impacts of light-induced degradation (LID). During light exposure, metastable defects form, but these can be partially remedied through annealing. The heating process enables hydrogen atoms to migrate and repair dangling bonds. Post-annealing, improvements in the open-circuit voltage ( $V_{oc}$ ) and short-circuit current density ( $J_{sc}$ ) are observed, indicating that annealing recovers some of the performance lost due to LID [60]. The Figure 4.3 shows how the number of dangling bonds decreases following annealing.

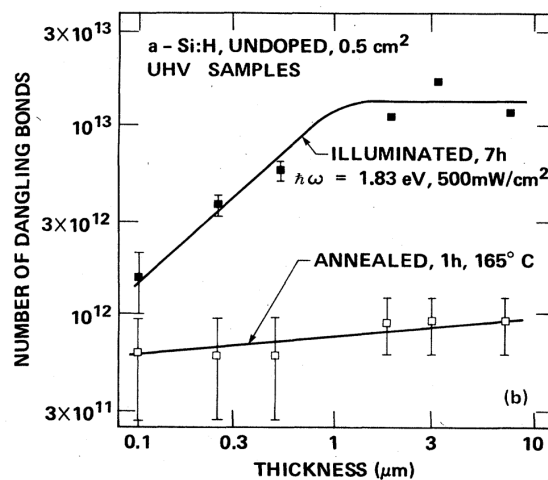


Figure 4.3: Thickness-dependent dangling bond concentration after light exposure and thermal treatment[60].

### 4.3. Methodology

This section outlines the comprehensive methodology for the LID study. Just as the fabrication process of p-SiC is detailed in Chapter 3, the Configurations of cells for the p-a-SiC single junction must first be described, with ample information provided on the various layers. Following this, the initial performance of the samples is evaluated. Next, the setup for the light soaking experiment is introduced. Lastly, the experimental design is elucidated through a flowchart.

#### 4.3.1. Configurations of cells

A set of samples, each consisting of 30 solar cells, was prepared on ASAHI U-type commercial glass strips. These samples were then coated with a layer of transparent conductive oxide (TCO), as shown in Figure 4.5. An intrinsic zinc oxide layer (i-ZnO) was applied as a buffer. The samples feature single-junction solar cells with p-a-SiC used as window layers. To minimize parasitic absorption, the thickness of the p-doped window layer is restricted to 16 nm. The structural breakdown of these two layers is depicted in Figure 4.4. Additionally, an intrinsic layer of a-Si is applied, requiring a thickness of 300 nm to enhance cell performance. After the single-junction p-i-n structure is completed, the back contact is then deposited.

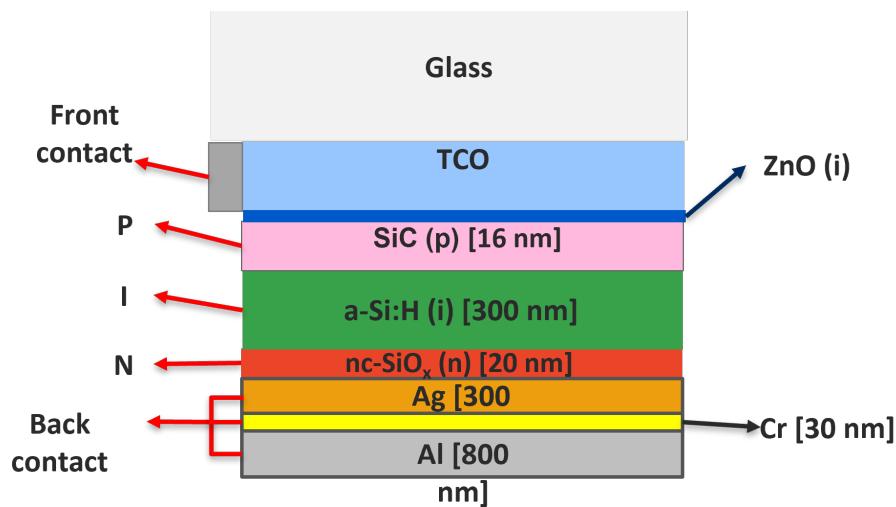


Figure 4.4: Device configuration of a-Si:H single junction solar cell with P-SiC window layer

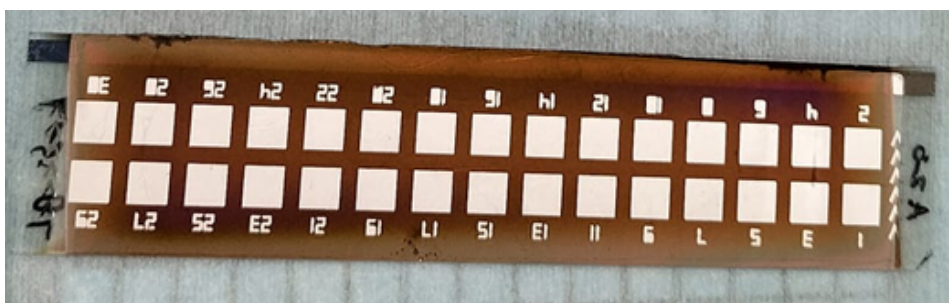


Figure 4.5: Sample with 30 cells.

The configuration of the nc-Si with a p-nc-SiOx window layer is detailed in Figure 4.6. Initially, the contact layer is laid down, consisting of a heavily doped nc-Si:OX (p+) material. Next, a buffer layer of SiOx(i) is applied, which sits between the p-doped layers and the intrinsic bulk. This buffer layer is designed to minimize recombination at the interface between the p-doped and intrinsic regions. On top of this, a 300 nm thick intrinsic bulk layer is deposited, followed by nc-Si:OX (n), which serves as the n-layer. This n-layer enhances conductivity and reduces parasitic absorption in the longer wavelength range.

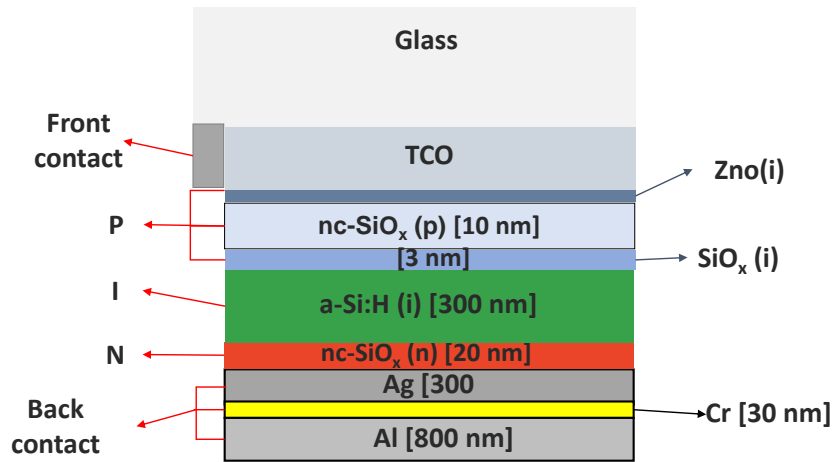


Figure 4.6: Device configuration of a-Si:H single junction solar cell with p-nc-SiOx window layer

The Figure 4.7 illustrates the configuration of two samples that use nc-Si as the intrinsic layer and p-nc-SiOx as the window layer. The only different layer of these samples is the TCO layer, in which one uses IOH as the TCO layer, and the other applies bi-layer TCO (iZnO+IOH). The purpose of utilizing these two configurations is to examine the performance of light-induced degradation after incorporating i-ZnO as the TCO layer. The investigation aims to determine whether degradation occurs at high energy wavelengths, as i-ZnO predominantly absorbs these wavelengths.

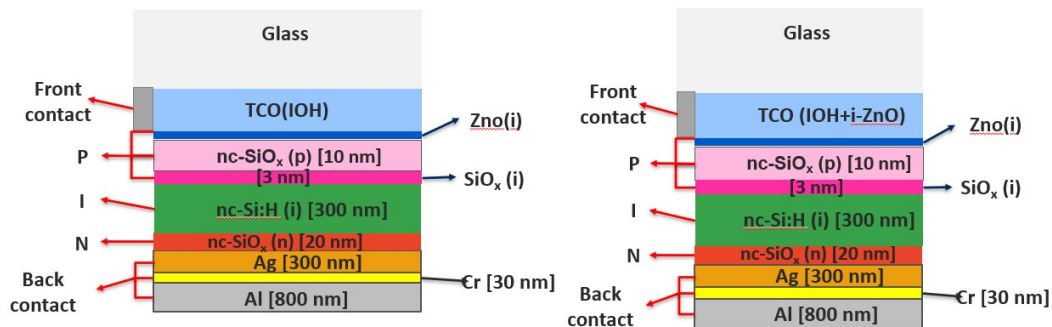


Figure 4.7: Device configuration of nc-Si:H single junction solar cell with P-nc-SiOx window layer

Micromorph configuration solar cells, being two phases of material, are a combination of amorphous silicon (a-Si:H) and nanocrystalline silicon(nc-Si:H) one after the other. The configuration of micromorph silicon thin film illustrated in Figure 4.8, the contact window layer are both p-nc-SiOx for the top and bottom cell, and the a-si:H and nc-si:H are intrinsic layers for the top and bottom cell respectively. The aim of this configuration is to see how affects the overall cell by controlling the thickness of the intrinsic bulk layer in both the top and bottom cells.

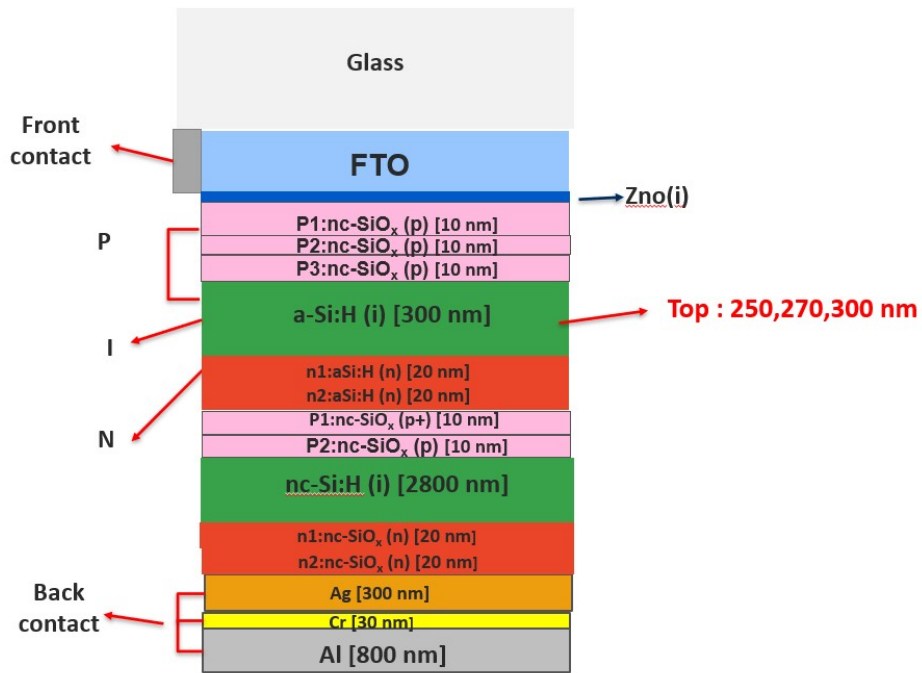


Figure 4.8: Device configuration of c-SiO<sub>x</sub>:H multi-junction solar cell with p-nc-SiO<sub>x</sub> window layer

### 4.3.2. Initial performance

The starting state of the solar cells is essential for performance evaluation, offering a reference point for comparison. It also provides insights into the material quality of the cells. In this experimental study, aimed at investigating how light soaking affects single-junction devices with different P-doping layers of a-Si, it is vital to first establish the initial performance of the cells. Prior to performance measurements, all samples are subjected to annealing at 180°C for 20 minutes. Since each sample comprises 30 solar cells, only the cell demonstrating the highest efficiency and open-circuit voltage will be chosen for the subsequent EQE analysis and measurement.

### 4.3.3. Light soaking experiment

The process of subjecting solar cell samples to light-induced degradation (LID) was carried out using the light-soaking system developed by the PVMD team at TU Delft. This system, depicted in Figure 4.9, involves positioning the samples on a stage that is illuminated by multiple metal halide lamps. To maintain the stage at a temperature of 50°C, deionized water is circulated through a cooling unit attached to the stage. Surrounding mirrors are used to reflect light onto the samples. The LID protocol adheres to IEC 61646 standards for light-soaking thin-film solar cells, with lamp power densities ranging from 700 to 720 W/m<sup>2</sup>. A high-sensitivity spectroradiometer is used to measure the light intensity.

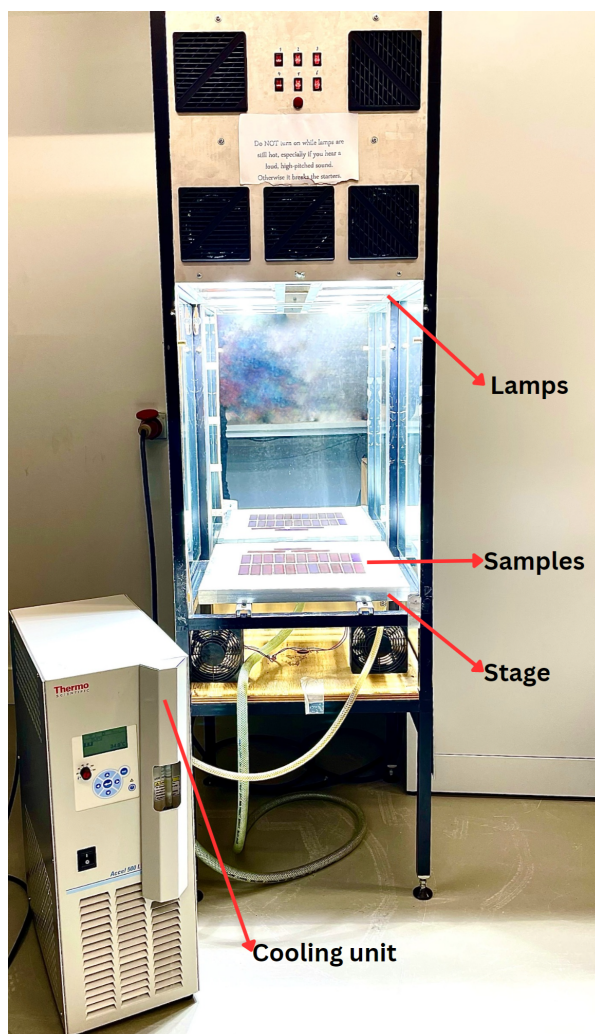


Figure 4.9: The set up of Light absorption experiment

#### 4.4. Design of experiments

The LID study was conducted through a series of experiments, necessitating careful consideration to understand how the results were derived. Figure 4.10 provides a flowchart detailing the entire experimental design for this study.

Initially, the samples underwent characterization after being annealed at 180°C for 20 minutes. This characterization included illuminated JV, EQE, and reflective measurements. For EQE measurement, the best-performing cell in the module, based on efficiency and open-circuit voltage, was selected.

Following this, the light soaking experiment was conducted for 20 minutes, after which the illuminated JV, EQE, and reflective measurements were repeated. This process, involving light soaking followed by cell characterization, was repeated throughout the study. The total light soaking time amounted to 1000 hours, with measurements taken at intervals of 20 minutes, 40 minutes, 60 minutes, 3 hours, 6 hours, 10 hours, 40 hours, 60 hours, 100 hours, 300 hours, 600 hours, and 1000 hours. To be mentioned, p-a-SiC only processes 600 hours of light absorption totally due to the equipment issue.

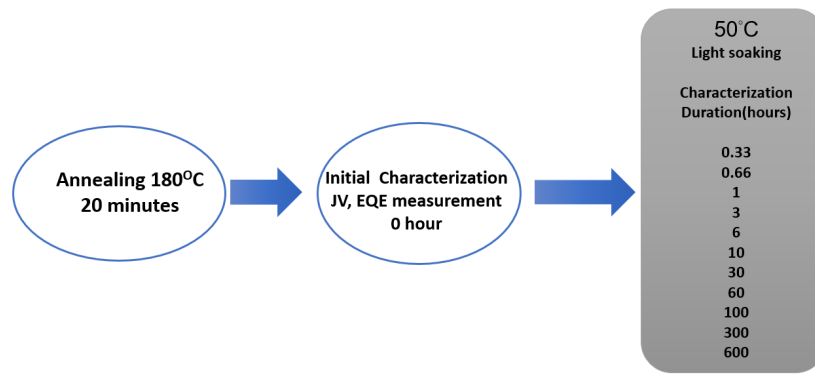


Figure 4.10: The flow chart of Light soaking experiment

## 4.5. Results and Discussion

### 4.5.1. LID on Solar cells with p doped Silicon Carbide as Window layer

**EQE characterisation:** The EQE of the solar cell offers a detailed understanding of the device's optical response and electrical losses. Consequently, the external quantum efficiency analysis reveals both the light absorption in the material and the behavior and movement of the light-induced charge carriers within the device. As previously noted, each sample contains 30 solar cells (or dots) with an area of 16 mm<sup>2</sup> per cell. Due to time constraints and equipment limitations, EQE measurements were performed on a single dot, selected for its superior initial performance throughout the experiments.

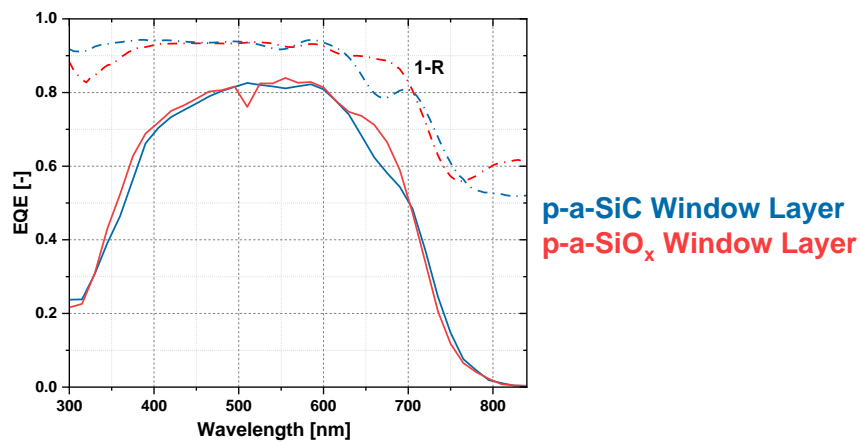


Figure 4.11: Initial performance of EQE and absorptance of SiC and SiOx

The Figure 4.11 illustrates the initial EQE performance between SiC and SiOx. It can be seen that the EQE of SiOx is better, especially in the blue region. This is due to the higher band gap energy of material of SiOx compared to SiC. This parasitic absorption may also be reduced by optimizing the thickness of p-layer. The 4.12 shows various EQEs as a function of the light soaking time. It can be seen that p-a-SiC:H suffers more performance drop due to LID than SiOx. The cell performance showed a sudden drop after 3 hours of light soaking. This suggest that the cell developed a parallel electrical shunt path. An overall EQE drop of p-a-SiC:H is due to this shunting of solar cells. There are two distinct perspectives regarding the cause of cell shunting. One perspective suggests that the issue may arise from a defect with the probes potentially damaging the solar cell's back contact by multiple measurements. Conversely, the other perspective attributes the problem to contaminants introduced during deposition, which could lead to cell shunting over time. Regardless of this, it is evident that the drop in the first

three hours of EQE is similar for both solar cells. This suggests that both solar cells might show the same mechanism of degradation in light absorption at the initial stages of light soaking.

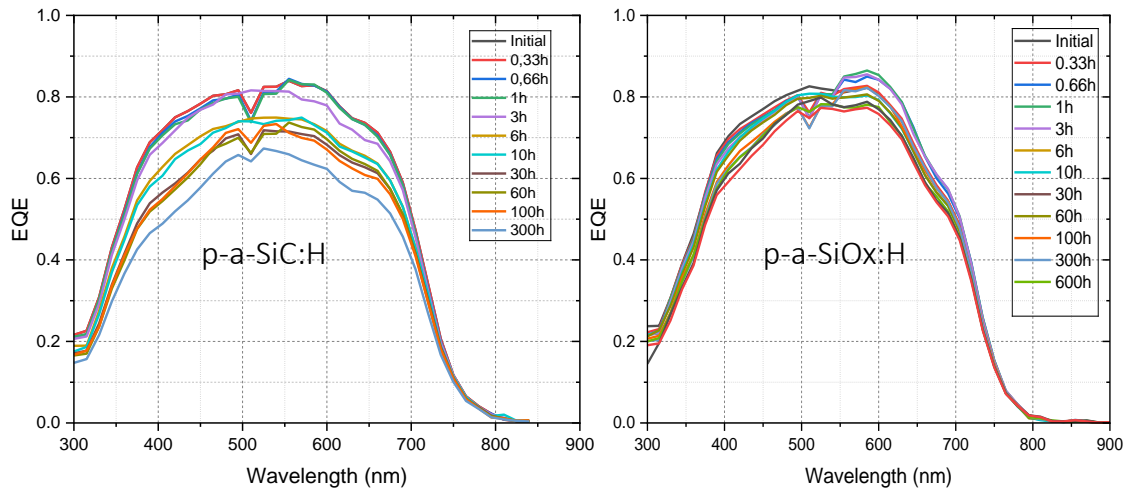


Figure 4.12: EQE of LID of p-a-SiC and p-a-SiOx window layer in amorphous silicon

#### Illuminated JV characterisation:

A solar cell's electrical performance can be greatly understood by studying the illuminated JV characterization. The Figure 4.11 illustrates the JV curve of p-a-SiC and p-a-SiOx during light soaking. As mentioned in the previous section, the p-a-SiC has a shunting issue which also can be seen from the Figure 4.11 that  $J_{sc}$  drops dramatically compared to p-a-SiOx. Furthermore, it also can be seen that both shunt resistance decrease and series resistance increase leading to the lower of the fill factor after degradation. The JV curve changes its shape as a trend over the measurements. Another impact that has to be noted for both the cells is that for SiC the  $V_{oc}$  remains the same, but for the ncSiOx cell, the  $V_{oc}$  drops over time. The  $V_{oc}$  drop can be considered as an effect of band bending related to degradation from the p-layer.

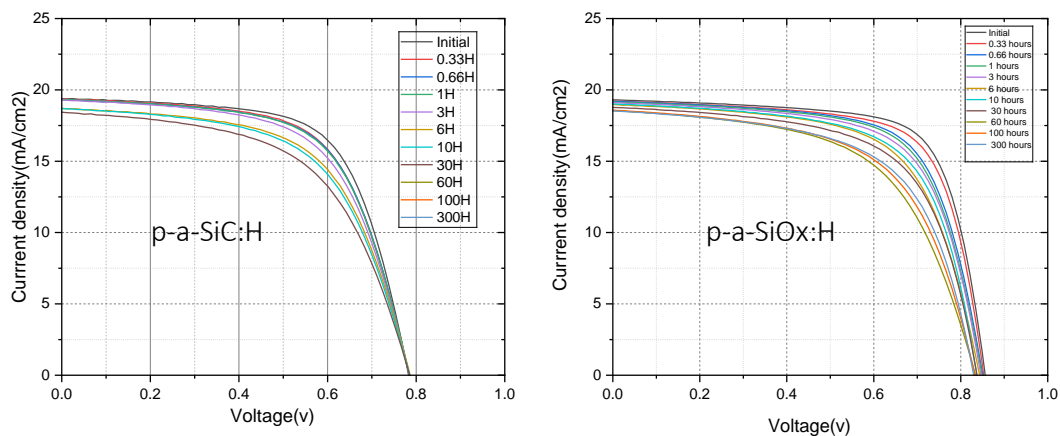


Figure 4.13: JV curve of p-a-SiC and p-a-SiOx window layer in amorphous silicon

#### External parameters:

Based on the outcomes of the light soaking experiments for silicon carbide, all the external parameters obtained from the JV characterization are individually plotted and compared. The  $J_{sc}$  plots are based on data obtained from EQE measurements. As a result, the  $J_{sc}$  data from EQE was also taken into account while making the efficiency plots. It shall be noted that the  $J_{sc}$  data from EQE characterization

is obtained by measuring the EQE of the best-performing cell out of the 30 cells in a sample. This limits the ability to plot the average data of the best-performing cells along with error bars. However, in order to observe the trends for more reliability, this has been attempted using a box plot on the external parameters apart from  $J_{sc}$  and efficiency.

Fill Factor (FF) is a measure of the electrical quality of a solar cell. It quantifies the maximum achievable power of the cell compared to the theoretical power if both the open-circuit voltage ( $V_{oc}$ ) and short-circuit current ( $I_{sc}$ ) were utilized optimally. In essence, FF is a ratio that compares the actual maximum power output of the solar cell to the product of  $V_{oc}$  and  $I_{sc}$ . The Figure 4.14 illustrates that p-nc-SiOx:H has a better fill factor for the initial and also after degradation. The fill factor of p-a-SiC decreases slowly within the first hour of light absorption, decreases faster afterward, and becomes stable after 100 hours of light soaking. In terms of p-nc-SiOx, it shows a similar trend in the fill factor decreasing slowly in the first hour of absorption, decreasing faster afterward, and reaching stable after 60 hours of absorption. Some of the points fluctuate in both p-a-SiC and p-nc-SiOx. However, the conclusion still can be made that both materials can reach stable fill factor after degradation which is different from the results of the Figure 4.15 that fill factor keeps suffering from degradation even after 600 hours. To be mentioned, some points like the 3hours measurement point of p-a-SiC and 6 hours measurement point of p-nc-SiOx have fluctuation this is due to the unstable JV measurement probably caused by the improper warming-up or calibration of the system, but the trend still can be referred to overall.

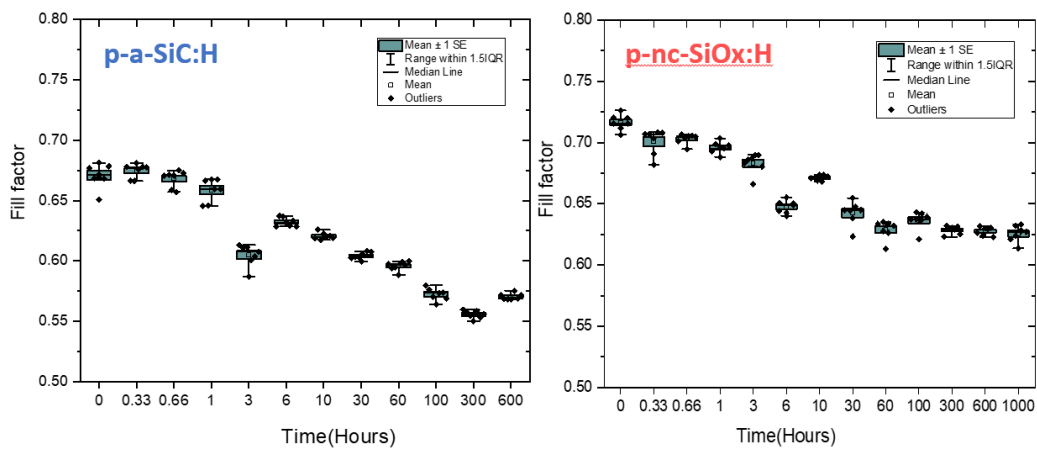


Figure 4.14: Fill factor for p-a-SiC and p-nc-SiOx window layer in amorphous silicon

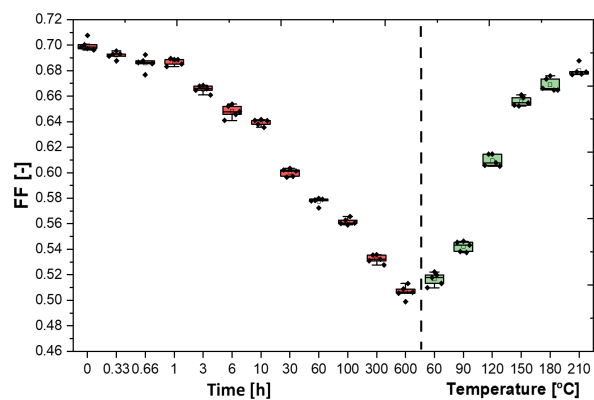


Figure 4.15: Fill factor for p-nc-SiOx window layer in amorphous silicon

**Open-circuit voltage ( $V_{oc}$ )** The value is a crucial indicator of a solar cell's potential to convert

sunlight into electrical energy. It is primarily influenced by the material properties of the semiconductor, such as the band gap energy, as well as the intensity and spectrum of the incident sunlight. The Figure 4.16 illustrates that p-a-SiO<sub>x</sub> has a better Voc for the initial and also after degradation due to a higher energy band gap. However, it also shows that the Voc of p-a-SiO<sub>x</sub> suffers more from the degradation than p-a-SiC. This might be due to the increase of the dangling-bond density of the intrinsic absorber layer which is faster for p-a-SiO<sub>x</sub> than p-a-SiC, which leads to a higher drop of Voc based on the study of [66].

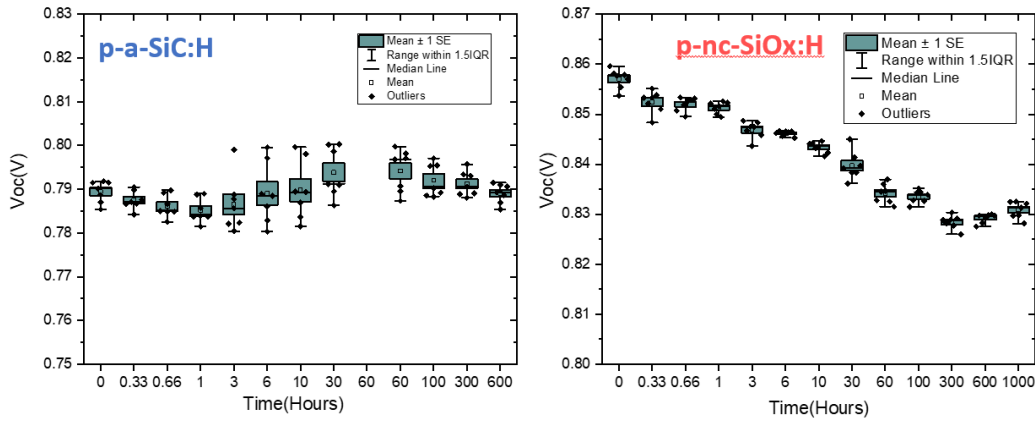


Figure 4.16: Voc for p-a-SiC and p-nc-SiO<sub>x</sub> window layer in amorphous silicon

**Series resistance(Rs)**

Series resistance represents the total resistance encountered by the current as it flows through the cell and its external connections. Series resistance is a critical parameter that impacts the efficiency and performance of solar cells. Minimizing is essential for improving the overall power conversion efficiency of photovoltaic devices. In general, higher series resistance leads to lower fill factor. Figure 4.17 illustrates the series resistance of SiC suffers more light-induced degradation than SiO<sub>x</sub>. Some reasons for series resistance increase after light absorption might be the degradation of contacts and interfaces, changes in material properties, and, degradation of TCO layers. Some of the points have fluctuations in both p-a-SiC and p-nc-SiO<sub>x</sub> due to a mismatch in setup during the JV measurement which makes the contact between the probe and solar cell not align with each other.

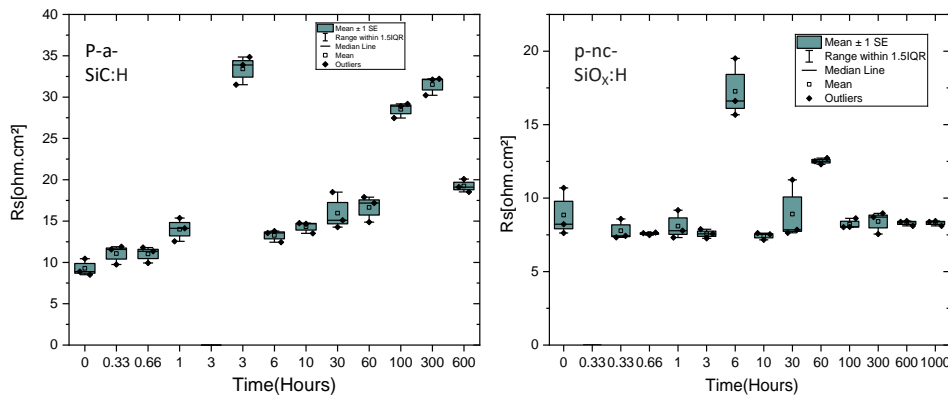


Figure 4.17: Series resistance of p-a-SiC and p-a-SiO<sub>x</sub> window layer in amorphous silicon

**Shunt resistance(Rsh)** Figure 4.17 illustrates the shunt resistance of p-a-SiC and p-nc-SiO<sub>x</sub> after light-induced degradation. It can be seen that the shunt resistance of both materials decreases after degradation which leads to a lower fill factor.

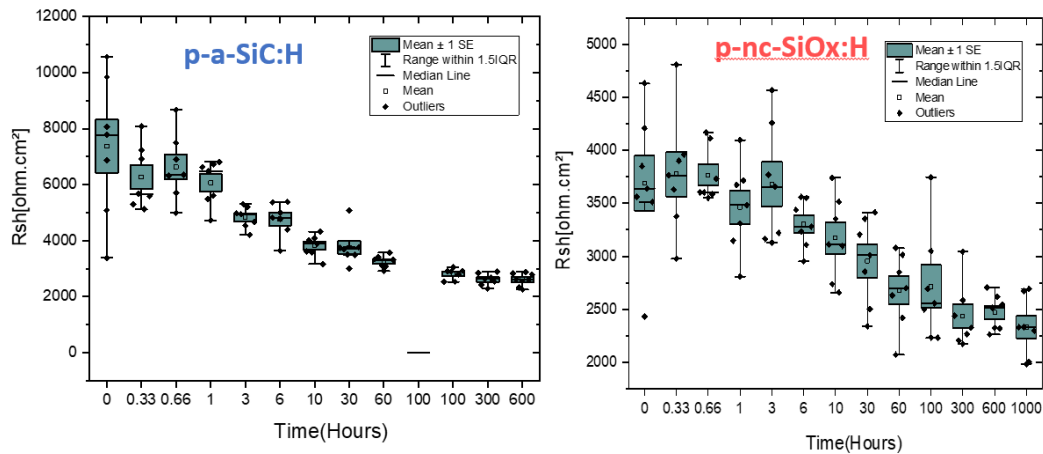


Figure 4.18: Shunt resistance of p-a-SiC and p-a-SiOx window layer in amorphous silicon

### Efficiency

Figure 4.19 illustrates the efficiency of p-a-SiC and p-nc-SiOx after light-induced degradation. It can be seen that the initial and after degradation efficiency of p-nc-SiOx is higher than p-a-SiC. This is a combined effect of the parameters and in SiC it is majorly due to Fillfactor and  $J_{sc}$  drop. In SiOx p layer solar cells, the  $J_{sc}$  drop is lower than SiC p layer solar cell but the change in  $V_{oc}$  is prominent. In terms of absolute value change, both p-a-SiC and p-nc-SiOx have around a 2.8% drop in efficiency after degradation of 600 hours.

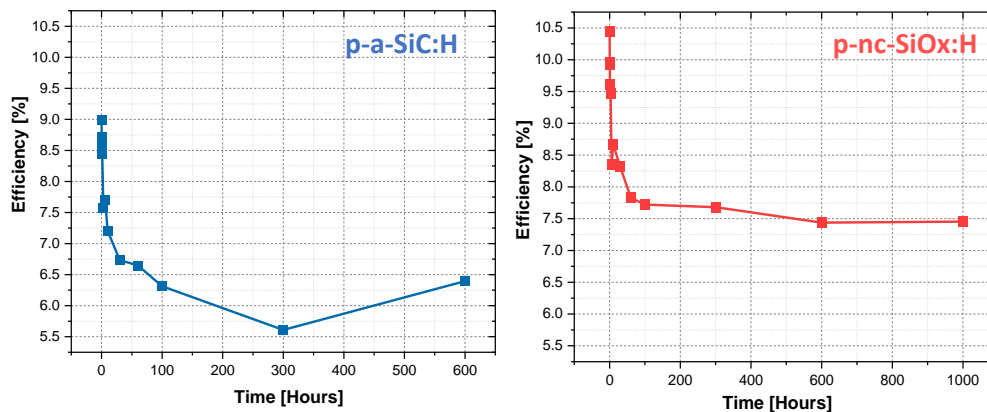


Figure 4.19: Efficiency of p-a-SiC and p-a-SiOx window layer in amorphous silicon

### 4.5.2. Effects of Light Exposure on Nanocrystalline Single Junction Solar cells

The optimal TCO is typically chosen by balancing transparency and conductivity. IOH and i-ZnO are selected as the ideal materials for this structure because of their excellent optoelectrical properties. A thin IOH layer guarantees high transparency in the visible spectrum and good lateral conductivity, while an additional i-ZnO layer minimizes parasitic absorption losses and ensures low transverse resistivity [67]. The high energy wavelength of light is mainly absorbed at iZnO, and from the EQE of light absorption experiment of p-a-SiOx in Figure 4.11, the degradation mainly is occurred in a higher energy wavelength. This experiment aims to see whether the light-induced degradation is optimized after applying a bi-layer that high energy wavelengths are absorbed by iZnO.

#### EQE characterisation:

The Figure 4.20 illustrates the initial performance of EQE and absorptance of TCO(IOH) and bilayer

TCO(IOH+iZnO) layers, it can be seen that the EQE of TCO(IOH) has better performance in the blue region due to the higher energy band gap. In contrast, the bilayer TCO(IOH+iZnO) has a better EQE performance in the overall and infrared region [68].

Moreover, the Figure 4.20 is the EQE after light-induced degradation. It can be seen that for TCO(IOH) the EQE curve does not suffer too much after degradation. Also, from the Figure 4.21 the absorbance ability of bilayer TCO(IOH+iZnO) is better than TCO(IOH) after degradation, it represents that the degradation of the EQE curve for bilayer TCO(IOH+iZnO) is probably caused by the shunting of the device instead of light-induced degradation.

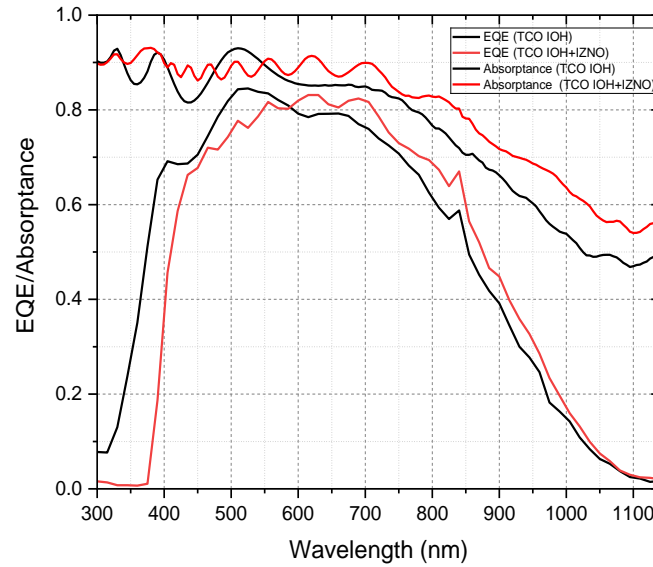


Figure 4.20: Initial performance of EQE and absorbance of TCO(IOH) and bilayer TCO(IOH+iZnO) layers

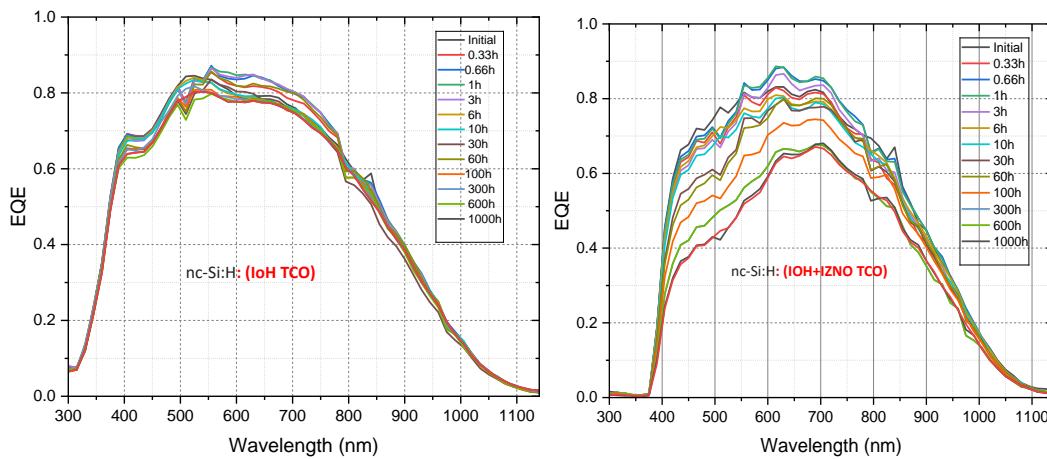


Figure 4.21: EQE of TCO(IOH) and bilayer TCO(IOH+iZnO) after degradation.

#### Illuminated JV characterisation:

The Figure 4.22 illustrates the initial and degradation JV curve between of TCO(IOH) and TCO (IOH+iZnO) layers, it can be seen that the bilayer TCO (IOH+iZnO) has a better initial Voc due to higher energy band gap, whereas the TCO(IOH) has slightly higher initial current density. It also can be seen that the series resistance increases after degradation for TCO(IOH). In terms of TCO (IOH+iZnO), series resistance increases and shunt resistance decreases after degradation. However, as mentioned before,

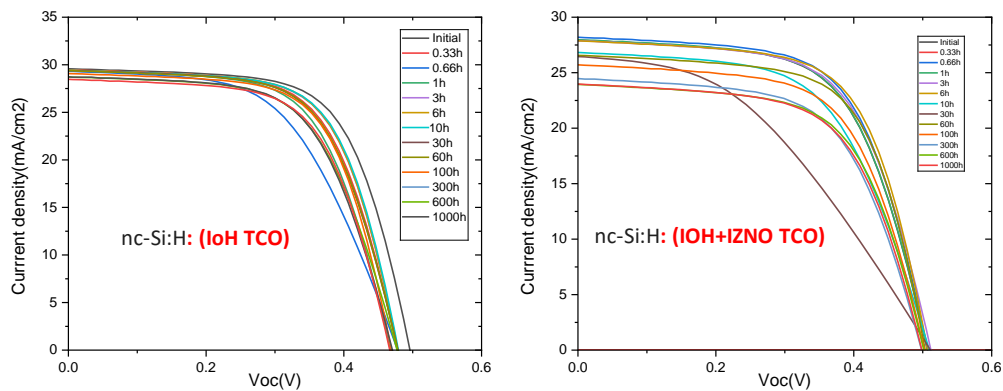


Figure 4.22: JV of TCO(IOH) and TCO (IOH+iZnO) layers

the nc-si:H with bilayer TCO (IOH+iZnO) has been shunted, so the conclusion can not be made that the degradation has been optimized after applying the bilayer TCO. TheFigure 4.23 illustrates that TCO(IOH) has a better fill factor.

**Open-circuit voltage (Voc)** TheFigure 4.24 illustrates that TCO (IOH+iZnO) layers have a better open-circuit voltage initially. The Voc does not reduce too much after degradation compared to a-si due to less defect density of nc-si:H which suffers less from light-induced degradation. This is reported that the higher the crystallinity of the intrinsic layer is, the less light-induced degradation is produced in solar cells [69]. This primarily occurs because the conduction and charge transfer in ncSi bulk happens exclusively through crystals in the solar cell.

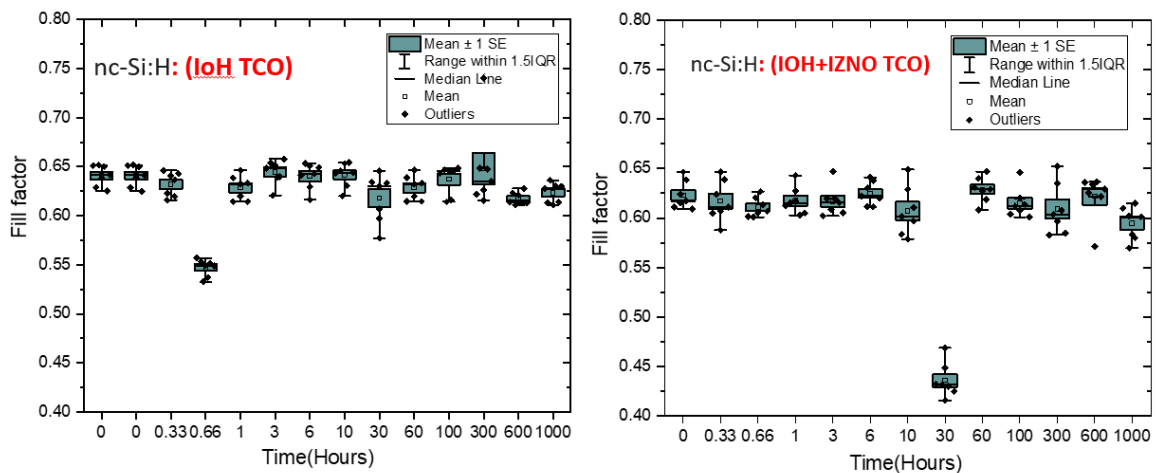


Figure 4.23: FF of TCO(IOH) and (IOH+iZnO) layers

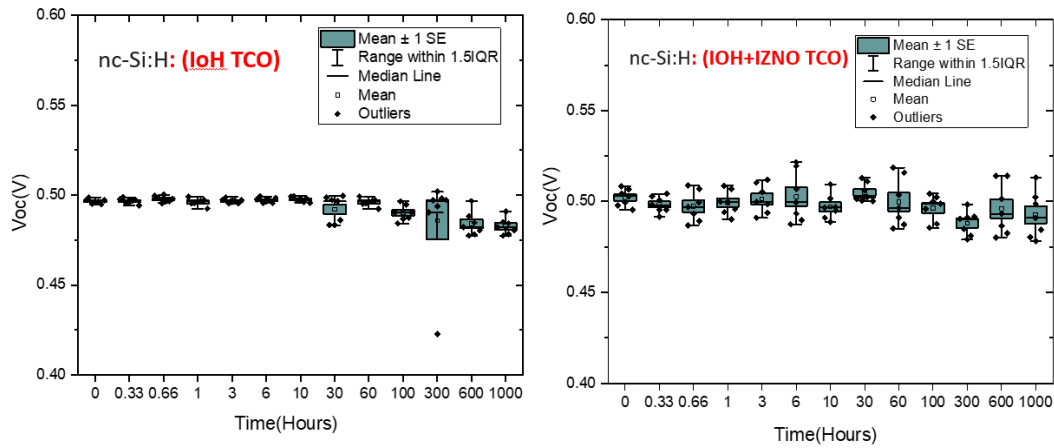


Figure 4.24: Voc of TCO(IOH) and (IOH+iZnO) layers

### Series resistance( $R_s$ )

The Figure 4.25 illustrates that Series resistance of TCO(IOH) and (IOH+iZnO) layers are almost the same. To be mentioned, some points like the 0.66-hour measurement point of TCO(IOH) and the 30-hour measurement point of (IOH+iZnO) layers have fluctuation this is due to the unstable JV measurement probably caused by the probe not touching the cell well during the process. The drop observed is null in both cases, implying the stability of TCO's under light and their ability to maintain charge transport. No layer in the total architecture of the solar cell is affected for charge transport and mobility as no major change in series resistance is observed.

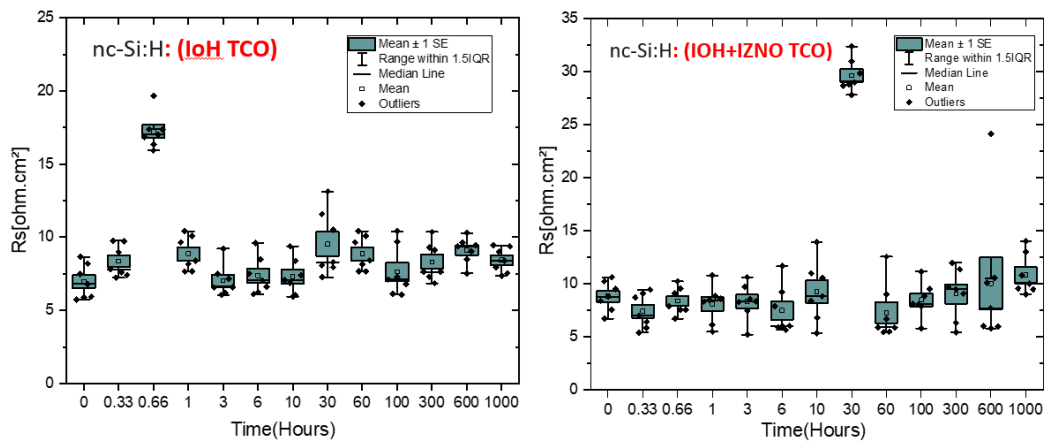


Figure 4.25: Series resistance of TCO(IOH) and (IOH+iZnO) layers

### Shunt resistance( $R_{sh}$ )

The Figure 4.26 illustrates that shunt resistance of TCO(IOH) is larger than bi-layer TCO (IOH+iZnO) layers. This might be due to the Bi-layer TCOs exhibiting higher roughness in the superstrate. Due to the sharp features, nanocrystalline bulk can cause cracks that act as shunt pathways, further reducing the shunt resistance compared to a single-layer IOH TCO. The single-layer TCO has flat IOH TCO which might cause a more uniform structure with fewer defects. In nanocrystalline solar cells, the charge carrier transport majorly takes place through crystals and light soaking doesn't seem to affect any crystal structure in the samples. As mentioned, some points like the 0.66-hour measurement point of TCO(IOH) and the 30-hour measurement point of (IOH+iZnO) layers have fluctuation this is due to the unstable JV measurement probably caused by the probe not touching the cell well during the process.

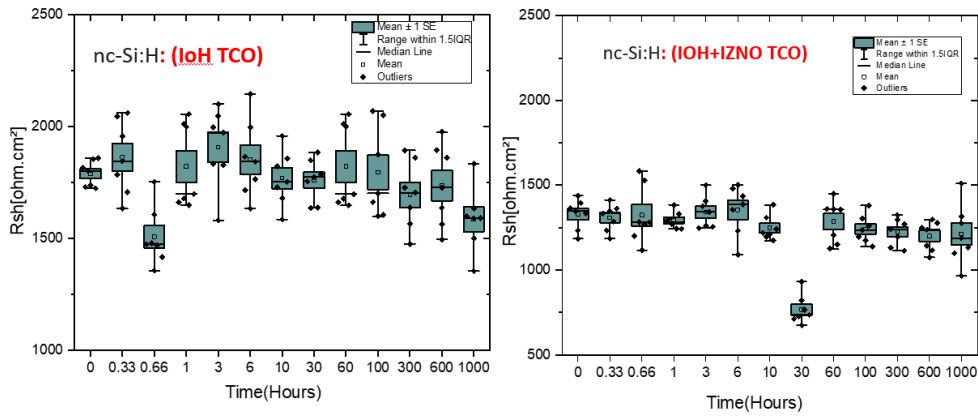


Figure 4.26: Shunt resistance of TCO(IOH) and (IOH+iZnO) layers

**Efficiency**

The Figure 4.27 illustrates that initial efficiency of TCO(IOH) is larger than bilayer TCO (IOH+iZnO) layers. The external parameters stay constant over the 600 hours of light soaking for both cells indicating that the nc-Si layers are not prone to any kind of degradation in electrical performance. The degradation of Efficiency is majorly contributed by optical response drop. This shall be also seen to stabilize with longer exposure to light. The efficiency seems to be stabilized with the stabilization of  $J_{sc}$ .

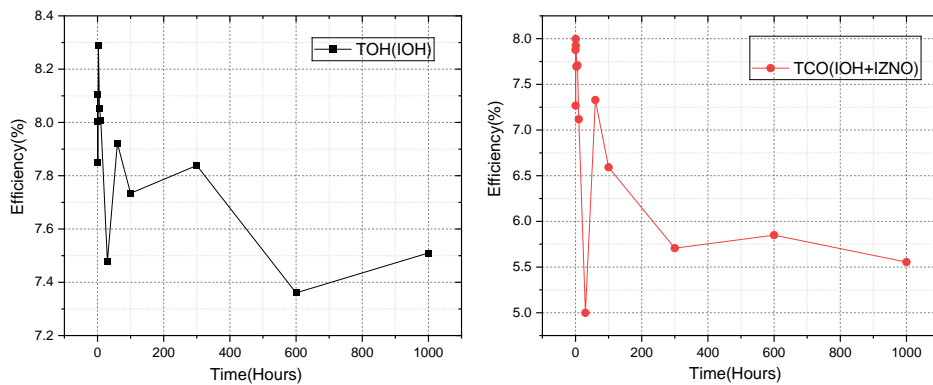


Figure 4.27: Efficiency of TCO(IOH) and (IOH+iZnO) layers

**4.5.3. LID on Solar cells with p-nc-SiOx as window layer on micromorph thin film**

The aim of investigating micromorph thin film is to see how much the  $J_{sc}$  of the top cell which uses amorphous silicon as an intrinsic layer drops after inducing degradation. A total of three samples with a thickness of the intrinsic layer as top cells 250nm, 270nm, and 300nm respectively are investigated.

The Figure 4.28 illustrates EQE for micromorph thin film on three samples. It can be seen that the top cell of the three samples suffers from degradation because amorphous silicon solar cell, whereas the bottom cell does not suffer too much from degradation due to nanocrystalline as an intrinsic layer. In general, the thinner the top cell, leaves more light for the bottom cell to utilize which makes the more degradation of the nanocrystalline solar cells. This matches the results of Figure 4.28, which the thicker one (M5) suffers less from the degradation of the nanocrystalline solar cells.

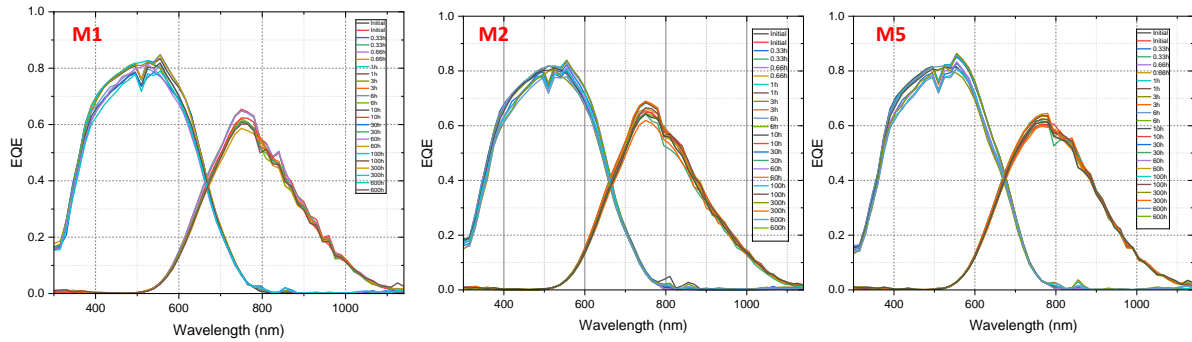


Figure 4.28: EQE for micromorph thin-film

### The short circuit current density of top cell and bottom cell in different light absorption time

	0	0.33h	0.66h	1 h	3h	6h	10	30h	60h	100h	300h	600h
M1												
Jsc ToC	12.2	12.7	14.2	14.3	14.3	13.8	13.8	13.6	13.7	13.4	13.5	13.4
Jsc BoC	10.6	10.8	11	10.9	11	10.4	10.4	10.3	10.4	10.3	10	10.2
M2												
Jsc ToC	13.8	13.9	14	14	14	13.6	13.6	13.3	13.4	13.5	13.3	13.1
Jsc BoC	11.3	11.6	11.7	11.7	11.7	11.2	11.2	10.9	11.3	11.4	10.6	11
M5												
Jsc ToC	14.5	14.5	14.5	14.5	14.4	14	13.9	13.8	13.8	13.7	13.7	13.6
Jsc BoC	11.0	11.2	11.3	11.3	11.4	10.8	10.8	10.9	11	11.1	10.8	10.9

The above tables illustrate the Jsc of the top cell and bottom cell in each measurement point. From the table, it can be seen that the top cell with a thickness of 270nm of intrinsic layer has an initial Jsc around 14.2 mA/cm<sup>2</sup> (The points at 0h and 0.33h can be neglected due to the unstable measurement). After degradation, the Jsc drops to 13.4 mA/cm<sup>2</sup> after 600 hours of light absorption, which has around 5.6% of Jsc. Similarly, the M2 with a thickness of 250 nm of intrinsic layer has Jsc around 6.4% (From initial 140 mA/cm<sup>2</sup> to 131 mA/cm<sup>2</sup>). Lastly, the M5 with a thickness 300 nm of intrinsic layer has Jsc about 6.2 % (From the original 145 mA/cm<sup>2</sup> to 136 mA/cm<sup>2</sup>). The results give some insights into how much of the Jsc of the top cell will drop after degradation which is around 6%. However, the micromorph thin film is still limited by the bottom cell of the nanocrystalline solar cell.

**Fill factor :** TheFigure 4.29 illustrates the Fill factor of three micromorph thin films. It can be seen that by manipulating the thickness of the top and bottom cells, a higher fill factor can be obtained in the M5 sample. Moreover, as mentioned before, the thinner the top cell, leaves more light for the bottom cell to utilize which causes more degradation of the nanocrystalline solar cell. The Fill factor of M2 with the thinner intrinsic layer of the top cell suffers the most after degradation due to the more degradation of the bottom cell which is the limited cell for micromorph thin films.

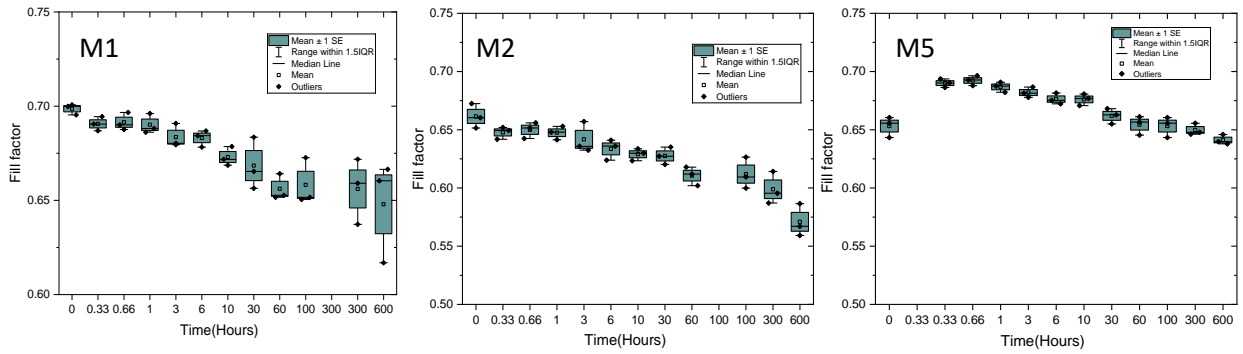


Figure 4.29: Fill factor for micromorph thin-film

**Open-circuit voltage (Voc):**

The Figure 4.30 illustrates the open circuit voltage of three micromorph thin films. It can be seen that all three samples have almost the same value of initial Voc. In terms of Voc after degradation, the sample with the thickest of top cells suffers slightly more than others. The Voc after degradation for micromorph thin film is not as serious as single junction solar cell. As mentioned before, the Voc of p-a-SiOx suffers more from degradation than p-nc-SiOx. In a micromorph thin film, more light reaches the bottom cell, which causes less degradation in the top cell compared to the single junction of p-a-SiOx.

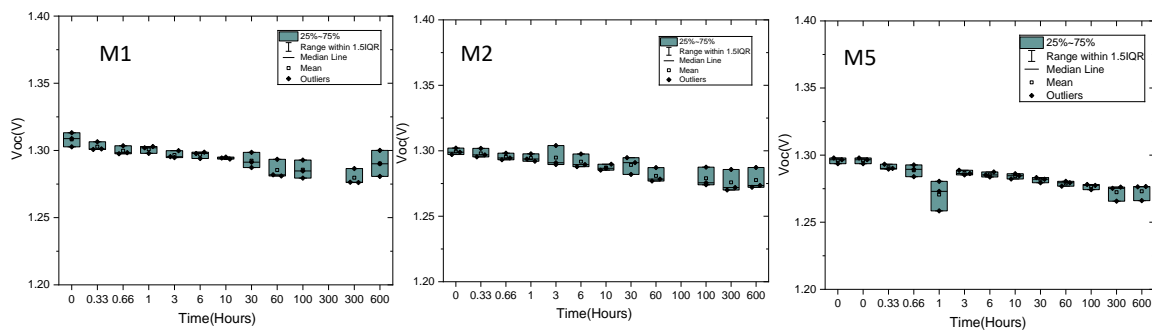


Figure 4.30: Open voltage for micromorph thin-film

**Series resistance(Rs):** The Figure 4.31 illustrates the series resistance of three micromorph thin films. which should not be varied with the different thicknesses of intrinsic layers. Based on the results, the series resistance of the micromorph thin film is higher than the single junction due to more layers of the configuration.

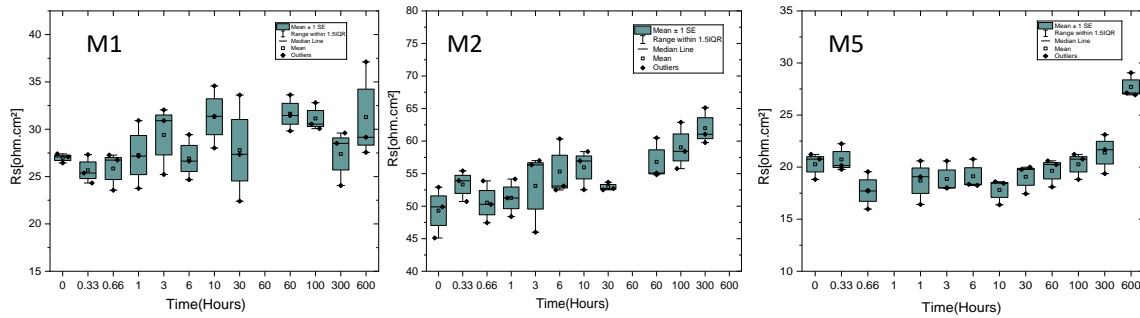


Figure 4.31: Series resistance for micromorph thin film

### Shunt resistance (Rsh):

The Figure 4.32 illustrates the Shunt resistance of three micromorph thin films, which can be seen that the thicker sample (M5) has the lowest shunt resistance. Also, the shunt resistance of the micromorph thin film is in the between of single junction of a-Si:H and nc-si:H. This might be because the crystal defect of micromorph thin films is in the middle of a-Si:H and nc-si:H, and the higher the crystal defect, the lower the shunt resistance.

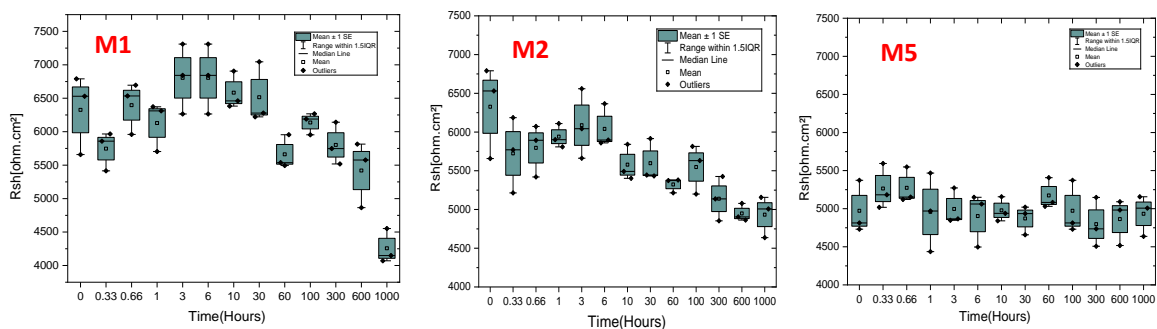


Figure 4.32: Shunt resistance for micromorph thin film

## 4.6. Summary

Based on the results of the light absorption experiment, the p-nc-SiOx has better EQE, open circuit voltage, and Fill factor than p-a-SiC. This is because the SiOx has a higher energy band gap than SiC. Furthermore, both p-nc-SiOx and p-a-SiC can reach a stable efficiency and fill factor, which contradicts the observation made in [41] where the performance was dropping even at 600 hours. About the difference of results in light-induced degradation of p-nc-SiOx, this needs to be further confirmed because sometimes the condition change during the fabrication might also affect the results.

The TCO bi-layer has a better EQE performance in the overall and Infrared area, whereas the TCO(IOH) has a better blue response due to a higher energy band gap. Both samples do not suffer too much from light-induced degradation which can be expected due to nanocrystalline as an intrinsic layer not suffering too much from LID.

In terms of the relationship between high energy wavelength and light-induced degradation, it can not be concluded due to the shunting issue of the p-nc-SiOx with the bi layer TCO.

Lastly, based on the results of the light absorption experiment of the micromorph thin film solar cell, it can be concluded that the top cell of amorphous silicon suffers from light-induced degradation whereas the bottom cell of nanocrystalline does not suffer too much from LID. The drop of Jsc for the top cell

---

after LID is around 6% for each cell, so to implement fill factor compensation, the sub-cells must be matched such that it has a 6% extra current in the top cell.

# Conclusions and Recommendations

## 5.1. Conclusions

Based on the findings from dark conductivity measurements and spectroscopic ellipsometry under various deposition parameters, the performance optimization focuses on achieving high conductivity, low activation energy, higher energy bandgap, and low reflectance and absorption. These factors contribute to obtaining high Voc and Jsc while minimizing parasitic absorption in p-SiC. To enhance solar cell performance, higher power and pressure in PECVD are employed, which in turn aids in accelerating the dissociation of B<sub>2</sub>H<sub>6</sub> and incorporation to the layers, thereby reducing activation energy and boosting dark conductivity. However, these conditions also result in a lower energy bandgap due to the rapid dissociation of SiH<sub>4</sub> compared to CH<sub>4</sub>. To counteract this, a higher CH<sub>4</sub> gas flow rate is used to increase the energy bandgap. Conversely, increasing CH<sub>4</sub> also raises activation energy and lowers dark conductivity. A higher B<sub>2</sub>H<sub>6</sub> gas flow rate is applied to decrease activation energy without significantly impacting the energy bandgap. Regarding refractive and extinction coefficients, reflectance and absorption are primarily material-dependent, indicating minimal influence from deposition parameters once the material is fully dissociated on the substrate. The receipt to obtain the optimal performance for p-SiC is at 9w, 1.1 mbar, SiH<sub>4</sub>:16 sccm, CH<sub>4</sub> 50 sccm, B<sub>2</sub>H<sub>6</sub> 15 sccm.

Based on the results, the p-nc-SiOx has better overall performance in EQE, Voc(0,83V), fill factor(0.625), and efficiency(7.5%). This is due to the higher band gap of p-nc-SiOx. Moreover, both p-nc-SiOx and p-a-SiC have reached a stable efficiency after 100 hours of light-induced degradation, with an overall loss of 28.5% compared to the initial efficiency. LID performance of the p-nc-SiOx window layer solar cell is similar to p-SiC window layer solar cell because it degrades less with around 28.5%, whereas p-SiC has a degradation of around 28.8% efficiency drop.

Based on the results of EQE, Solar cells with two-layer TCO (IOH-iZnO) have a better EQE performance in the green region and also the infrared area, whereas the TCO (IOH) has a better blue response due to a higher energy band gap of IOH. From the reflection of solar cells after degradation, we conclude that both of the cells suffer less from light-induced degradation than a-si:H which can be expected. However, it can not be concluded whether the degradation mainly occurred because of the high energy wavelength due to the shunting of p-nc-SiOx with two-layer TCO (IOH-iZnO).

Based on the results of micromorph thin film solar cells, the solar cells with bottom cell(nc-si:H) limited current, have better fill factor and suffer less from degradation. This results in an overall better performance of the solar cell. The current drop of amorphous silicon in a top cell for each sample is around 6% of the initial current after degradation. Thus to implement current matching, the subcells must be matched such that it has a 6% extra current in the top cell.

## 5.2. Recommendations

After optimization of the boron-doped SiC layer, the efficiency of a single junction solar cell after applying p-sic as a window layer was around 8.2%, which still requires further optimization to obtain higher efficiency. This might be achieved by applying the buffer layer at the p/i interface to increase the VoC and efficiency.

Secondly, based on the results of JV measurement and EQE measurement, the cells suffer from shunting issues, which affects the reliability of results. The shunting issues may result from multiple measurements by the measuring setup. Addressing these problems can greatly improve result accuracy, reducing the errors compared to the results included in this report.

Also, the process of optimization of layers requires a stable PECVD. It has been noted that the reflection power of the equipment is massive for some depositions. This will also lead to different results. However, the key to obtaining good performance of layers is to make the optical and electrical performance in a specific range. In our experiment, the energy band gap is around 2.1(eV), and the activation is 0.385(eV). It can be concluded that making the depositions stable in the PECVD can enhance the performance of layers in future depositions.

# References

- [1] Barry C Brusso. "A brief history of the energy conversion of light [history]". In: *IEEE Industry Applications Magazine* 25.4 (2019), pp. 8–13.
- [2] Jason Svarc. "Most efficient solar panels 2021". In: *Clean Energy Reviews: Dulwich Hill, Australia* (2020).
- [3] S Peake. "Renewable energy-power for a sustainable future." In: (2018).
- [4] Martin A Green. "Solar cell efficiency tables". In: *Prog. Photovoltaic Res. Applic.* 8 (2000).
- [5] Rebert W Miles, Kathleen M Hynes, and Ian Forbes. "Photovoltaic solar cells: An overview of state-of-the-art cell development and environmental issues". In: *Progress in crystal growth and characterization of materials* 51.1-3 (2005), pp. 1–42.
- [6] E Płaczek-Popko. "Top PV market solar cells 2016". In: *Opto-Electronics Review* 25.2 (2017), pp. 55–64.
- [7] Rui Zhu, Zhongwei Zhang, and Yulong Li. "Advanced materials for flexible solar cell applications". In: *Nanotechnology Reviews* 8.1 (2019), pp. 452–458.
- [8] Ka-Hyun Kim, Erik V Johnson, and Pere Roca i Cabarrocas. "Irreversible light-induced degradation and stabilization of hydrogenated polymorphous silicon solar cells". In: *Solar Energy Materials and Solar Cells* 105 (2012), pp. 208–212.
- [9] K Vasilevskiy and NG Wright. "Historical introduction to silicon carbide discovery, properties and technology". In: *Advancing Silicon Carbide Electronics Technology II: Core Technologies of Silicon Carbide Device Processing* 69.1 (2020).
- [10] J Dong and A-B Chen. "Fundamental properties of SiC: crystal structure, bonding energy, band structure, and lattice vibrations". In: *SiC Power Materials: Devices and Applications*. Springer, 2004, pp. 63–87.
- [11] Po-Chih Chen et al. "Defect inspection techniques in SiC". In: *Nanoscale Research Letters* 17.1 (2022), p. 30.
- [12] Swapnadip De. "Basic Semiconductor and Metal-Oxide-Semiconductor (MOS) Physics". In: *Technology Computer Aided Design*. CRC Press, 2018, pp. 61–160.
- [13] A Wallace Copeland, Otis D Black, and AB Garrett. "The Photovoltaic Effect." In: *Chemical reviews* 31.1 (1942), pp. 177–226.
- [14] Gil Knier. "How do photovoltaics work". In: *Science@ NASA* (2002).
- [15] Arno Smets et al. "Solar Energy: The physics and engineering of photovoltaic conversion, technologies and systems". In: (2016).
- [16] Donald A Neamen and Dhruvas Biswas. "Semiconductor physics and devices". In: (2011).
- [17] Gavin Conibeer. "Third-generation photovoltaics". In: *Materials today* 10.11 (2007), pp. 42–50.
- [18] Peter Würfel and Uli Würfel. "Physics of solar cells: from basic principles to advanced concepts". In: (2016).
- [19] Mohammad OMID and ÖMER CORA. "State of the art review on the Cu (In, Ga) Se<sub>2</sub> thinfilm solar cells". In: *Turkish Journal of Electromechanics and Energy* 5.2 (2020).
- [20] Robert Street. *Technology and applications of amorphous silicon*. Vol. 37. Springer Science & Business Media, 1999.
- [21] RA Street. "Hydrogen density of states model for amorphous silicon and alloys". In: *MRS Online Proceedings Library (OPL)* 219 (1991), p. 253.
- [22] S Sreejith et al. "A comprehensive review on thin film amorphous silicon solar cells". In: *Silicon* 14.14 (2022), pp. 8277–8293.

- [23] Jimmy Melskens et al. "Migration of open volume deficiencies in hydrogenated amorphous silicon during annealing". In: *IEEE Journal of Photovoltaics* 7.2 (2017), pp. 421–429.
- [24] Bas Vet. "Improvement of a-Si: H devices by analysis, simulations and experiment". In: (2014).
- [25] Marinus Fischer et al. "High pressure processing of hydrogenated amorphous silicon solar cells: Relation between nanostructure and high open-circuit voltage". In: *Applied Physics Letters* 106.4 (2015).
- [26] Ruud EI Schropp et al. "Metastability". In: *Amorphous and Microcrystalline Silicon Solar Cells: Modeling, Materials and Device Technology* (1998), pp. 99–113.
- [27] Na Wang et al. "Light soaking of hydrogenated amorphous silicon: a short review". In: *Carbon Neutrality* 3.1 (2024), p. 18.
- [28] 1\_D L Staebler and CR Wronski. "Reversible conductivity changes in discharge-produced amorphous Si". In: *Applied physics letters* 31.4 (1977), pp. 292–294.
- [29] Md Nazmul Islam Sarkar and Himangshu Ranjan Ghosh. "Efficiency improvement of amorphous silicon single junction solar cell by design optimization". In: *2017 International Conference on Electrical, Computer and Communication Engineering (ECCE)*. IEEE, 2017, pp. 670–675.
- [30] Ritesh Jaiswal, Anil Kumar, and Anshul Yadav. "Nanomaterials based solar cells". In: *Nanotechnology in the Automotive Industry*. Elsevier, 2022, pp. 467–484.
- [31] Arvind Shah. "Thin-film silicon solar cells". In: *Practical Handbook of Photovoltaics*. Elsevier, 2012, pp. 209–281.
- [32] ARUN MADAN. "Amorphous Silicon Solar Cells". In: *Materials Processing: Theory and Practices* 5 (1985), pp. 331–375.
- [33] Miro Zeman and J Krc. "Optical and electrical modeling of thin-film silicon solar cells". In: *Journal of Materials Research* 23.4 (2008), pp. 889–898.
- [34] Ramakrishna Madaka et al. "Tunnel recombination junction influence on the a-Si: H/SHJ tandem solar cell". In: *Materials Today: Proceedings* 39 (2021), pp. 1970–1973.
- [35] Yasaman Hamedani et al. "Plasma-enhanced chemical vapor deposition: where we are and the outlook for the future". In: *Chemical Vapor Deposition-Recent Advances and Applications in Optical, Solar Cells and Solid State Devices* 4 (2016), pp. 243–280.
- [36] AHM Smets and MCM Van De Sanden. "Relation of the Si H stretching frequency to the nanostructural Si H bulk environment". In: *Physical Review B* 76.7 (2007), p. 073202.
- [37] Sandeep Arya and Prerna Mahajan. "Characterization Techniques". In: *Solar Cells: Types and Applications*. Springer, 2023, pp. 211–235.
- [38] Enric Garcia-Caurel et al. "Application of spectroscopic ellipsometry and Mueller ellipsometry to optical characterization". In: *Applied spectroscopy* 67.1 (2013), pp. 1–21.
- [39] Gerald E Jellison. "Data analysis for spectroscopic ellipsometry". In: *Handbook of Ellipsometry*. Springer, 2005, pp. 237–296.
- [40] I Martil and G Gonzalez Diaz. "Determination of the dark and illuminated characteristic parameters of a solar cell from IV characteristics". In: *European journal of physics* 13.4 (1992), p. 193.
- [41] Shriram Muthaiyan Karthikeyen. "Effects of light soaking on the performance and stability of a-Si: H thin-film solar cells". In: (2023).
- [42] Man Xu et al. "Recent advances and challenges in silicon carbide (SiC) ceramic nanoarchitectures and their applications". In: *Materials Today Communications* 28 (2021), p. 102533.
- [43] CM Fortmann et al. "Light induced degradation and structure of high efficiency a-Si: H, a-SiGe: H and a-SiC: H solar cells". In: *AIP Conference proceedings*. Vol. 157. 1. American Institute of Physics, 1987, pp. 103–110.
- [44] Kichan Yoon et al. "Preparation and characterization of p-type hydrogenated amorphous silicon oxide film and its application to solar cell". In: *Journal of non-crystalline solids* 357.15 (2011), pp. 2826–2832.

- [45] M Fernandes et al. "Automated PECVD System for Fabrication of a-Si: H Devices". In: *Procedia Technology* 17 (2014), pp. 580–586.
- [46] Thanh H Nguyen and Stephen K O'Leary. "The dependence of the Fermi level on temperature, doping concentration, and disorder in disordered semiconductors". In: *Journal of Applied Physics* 88.6 (2000), pp. 3479–3483.
- [47] C Ilescu et al. "Residual stress in thin films PECVD depositions". In: *Journal of Optoelectronics and Advanced Materials* 13.4 (2011), pp. 387–394.
- [48] C Summonte et al. "Boron doping of silicon rich carbides: Electrical properties". In: *Materials Science and Engineering: B* 178.9 (2013), pp. 551–558.
- [49] C Baron et al. "Cathodoluminescence of highly and heavily boron doped (100) homoepitaxial diamond films". In: *Diamond and related materials* 15.4-8 (2006), pp. 597–601.
- [50] HO Yadav. "Relation between the thermal activation energy of conduction and the first excited singlet state energy—a case of photo-conducting organic materials". In: *Thin solid films* 477.1-2 (2005), pp. 222–226.
- [51] Shui-Yang Lien et al. "Effects of RF power and pressure on performance of HF-PECVD silicon thin-film solar cells". In: *Thin Solid Films* 518.24 (2010), pp. 7233–7235.
- [52] Noura D Alkhalidi, Sajib K Barman, and Muhammad N Huda. "Crystal structures and the electronic properties of silicon-rich silicon carbide materials by first principle calculations". In: *Heliyon* 5.11 (2019).
- [53] Bruno Lopez-Rodriguez et al. "High-Quality Amorphous Silicon Carbide for Hybrid Photonic Integration Deposited at a Low Temperature". In: *ACS photonics* 10.10 (2023), pp. 3748–3754.
- [54] J Zemek et al. "Surface and in-depth distribution of sp<sup>2</sup> and sp<sup>3</sup> coordinated carbon atoms in diamond-like carbon films modified by argon ion beam bombardment during growth". In: *Carbon* 134 (2018), pp. 71–79.
- [55] Shuyan Shao and Maria Antonietta Loi. "The role of the interfaces in perovskite solar cells". In: *Advanced Materials Interfaces* 7.1 (2020), p. 1901469.
- [56] Zhao-Kui Wang and Liang-Sheng Liao. "Doped charge-transporting layers in planar perovskite solar cells". In: *Advanced Optical Materials* 6.17 (2018), p. 1800276.
- [57] Erkan Aydin, Michele De Bastiani, and Stefaan De Wolf. "Defect and contact passivation for perovskite solar cells". In: *Advanced Materials* 31.25 (2019), p. 1900428.
- [58] Erteza Tawsif Efaz et al. "A review of primary technologies of thin-film solar cells". In: *Engineering Research Express* 3.3 (2021), p. 032001.
- [59] AF Meftah, AM Meftah, and A Merazga. "Created defect under illumination in a-Si: H: hydrogenated or isolated dangling bond?" In: *Vacuum* 75.3 (2004), pp. 269–273.
- [60] 7\_M Stutzmann, WB Jackson, and CC Tsai. "Light-induced metastable defects in hydrogenated amorphous silicon: A systematic study". In: *Physical Review B* 32.1 (1985), p. 23.
- [61] Howard M Branz. "Hydrogen collision model: Quantitative description of metastability in amorphous silicon". In: *Physical Review B* 59.8 (1999), p. 5498.
- [62] Jimmy Melskens, Nikolas J Podraza, and Michael E Stuckelberger. "Infrared optical properties: Hydrogen bonding and stability". In: *The World Scientific Reference of Amorphous Materials: Structure, Properties, Modeling and Main Applications: Volume 3 Structure, Properties, and Applications of Tetrahedrally Bonded Thin-Film Amorphous Semiconductors*. World Scientific, 2021, pp. 85–128.
- [63] Jimmy Melskens. "Hydrogenated amorphous silicon: nanostructure and defects". In: (2015).
- [64] Subhendu Guha et al. "High quality amorphous silicon materials and cells grown with hydrogen dilution". In: *Solar energy materials and solar cells* 78.1-4 (2003), pp. 329–347.
- [65] Kim SOLESVIK Oppedal. "A Study of the Staebler-Wronski Effect and Amorphous Silicon Solar Cells". In: *Delft University of Technology* (2013).
- [66] Michael Stuckelberger et al. "Light-induced Voc increase and decrease in high-efficiency amorphous silicon solar cells". In: *Journal of Applied Physics* 116.9 (2014).

- 
- [67] Prashand Kalpoe. "Transparent conductive oxide bi-layer as front contact for multijunction thin film silicon photovoltaic cells". In: (2023).
- [68] Federica Saitta et al. "Transparent Conductive Oxide Bi-Layer as Front Contact for Multijunction Thin-Film Silicon Solar Cells". In: *2023 IEEE 50th Photovoltaic Specialists Conference (PVSC)*. IEEE, 2023, pp. 1–3.
- [69] Yan Wang et al. "Light induced degradation of microcrystalline silicon solar cells". In: *Journal of non-crystalline solids* 352.9-20 (2006), pp. 1909–1912.